

VLBI Polarimetry of 177 Sources from the Caltech-Jodrell Bank Flat-spectrum Survey

L. K. Pollack,^{1,2} G. B. Taylor,¹ R. T. Zavala¹

lpollack@uclink4.berkeley.edu, gtaylor@nrao.edu, rzavala@nrao.edu

ABSTRACT

We present VLBA observations and a statistical analysis of 5 GHz VLBI polarimetry data from 177 sources in the Caltech-Jodrell Bank flat-spectrum (CJF) survey. The CJF survey, a complete, flux-density-limited sample of 293 extragalactic radio sources, gives us the unique opportunity to compare a broad range of source properties for quasars, galaxies and BL Lacertae objects. We focus primarily on jet properties, specifically the correlation between the jet axis angle and the polarization angle in the core and jet. A strong correlation is found for the electric vector polarization angle in the cores of quasars to be perpendicular to the jet axis. Contrary to previous claims, no correlation is found between the jet polarization angle and the jet axis in either quasars or BL Lac objects. With this large, homogeneous sample we are also able to investigate cosmological issues and AGN evolution.

Subject headings: galaxies: active – galaxies: jets – galaxies: nuclei – radio continuum: galaxies; polarimetry

1. Introduction

Studies of the polarization properties of jets on the milliarcsecond scale can yield vital insights about their formation, collimation, and propagation (e.g. Gómez et al. 2000; Meier

¹National Radio Astronomy Observatory, P.O. Box 0, Socorro, NM 87801

²University of California, Berkeley, Berkeley, CA 94704

2001). Based on results from 25 BL Lacs, Gabuzda, Pushkarev & Cawthorne (2000) claim a tendency for the electric vector polarization angle to lie along the jet axis for these objects, with about 30 percent showing a perpendicular orientation. This has been interpreted in terms of oblique and transverse shocks (Gabuzda, Pushkarev & Cawthorne 2000) or as the result of a helical magnetic field confining the jet (Gabuzda 2002).

Although many individual sources and even large surveys have been undertaken with VLBI in total intensity, the number of sources studied with VLBI polarimetry is far less. In the early years of VLBI this was due in part to hardware restrictions (e.g., feeds with only a single available polarization), but also due to software restrictions that made calibration difficult. The VLBI group at Brandeis pioneered efforts to develop techniques and software to make VLBI polarimetry more tractable (Roberts et al. 1984; Roberts, Brown, & Wardle 1991), and this culminated in a study of the mas polarization structure of 24 sources from the Pearson-Readhead sample (Cawthorne et al. 1993). But it wasn't until the advent of the VLBA, with homogeneous, low-leakage antennas and feeds, that VLBI polarimetry became widely accessible. Full polarization calibration techniques were implemented in AIPS in the 1990s and in 1999 NRAO began providing regular monitoring³ of a suite of calibrators that can be used for the absolute polarization angle calibration (Taylor & Myers 2000).

The Caltech-Jodrell Bank flat-spectrum (CJF) survey is a large complete, flux-limited sample of sources imaged with VLBI, consisting of 293 sources (Taylor et al. 1996). This survey has been used to place constraints on gravitational lensing by $10^5 M_{\odot}$ black holes (Wilkinson et al. 2001), to study the unbeamed synchrotron luminosities of relativistic jets (Lister & Marscher 1997), and recently to study the relation between the linear size of the VLBI jet and the black hole mass (Cao & Jiang 2002).

As part of a proper-motion study of compact objects, all the sources in the CJF sample were observed at least 3 times at intervals of approximately 2 years (Britzen et al. 1998). The early epochs used Global VLBI observations, but starting in 1995 the VLBA was used exclusively since it could provide better (u, v) coverage and consequently improved image fidelity. The first observing sessions with the VLBA were limited in bandwidth (8 MHz) and used only a single polarization, but as the VLBA matured and its capabilities increased, we began in 1998 to observe with 16 MHz bandwidth in full polarization mode. The last three epochs of CJF were observed in this mode and provide full VLBI polarimetry of 177 sources.

Here we present a statistical analysis of the properties of those 177 sources in CJF observed with full polarimetry. The sample is described in detail in §2, and the calibration procedures are described in §3. We present results in §4, and discuss comparisons of source

³<http://www.aoc.nrao.edu/~smyers/calibration/>

properties, and evolution of those properties with redshift in §5.

We assume $H_0 = 75 \text{ km s}^{-1} \text{ Mpc}^{-1}$ and $q_0=0.5$ throughout.

2. Sample Selection

We present 5 GHz Very Long Baseline Interferometric (VLBI) polarimetry observations of 177 sources in the Caltech-Jodrell Bank flat-spectrum (CJF) survey, a complete flux-density-limited sample of 293 flat-spectrum radio sources. The CJF sample requires that the flux density at 4850 MHz be at least 350 mJy, ($S_{4850} \geq 350 \text{ mJy}$), and that the spectral index at 4850 MHz and 1400 MHz be at least -0.5 ($\alpha_{1400}^{4850} \geq -0.5$). Additionally, the sample is limited by B1950 declinations and galactic latitudes such that $\delta \geq 35^\circ$ and $|b| \geq 10^\circ$. A list of the 293 extragalactic radio sources and a more complete description of the selection criteria for the CJF sample can be found in Taylor et al. (1996). The CJF sample has been completely observed with VLBI as part of the PR (Pearson & Readhead 1988), CJ1 (Polatidis et al. 1995) and CJ2 (Taylor et al. 1994) surveys.

The 177 sources presented here were observed as part of a proper motion study (Britzen et al. 1998) so that polarimetric data in multiple epochs are available for 66 of the 177 sources. Where data from multiple epochs was available, we preferred the 2000.958 observations over the 1998.122 observations, and used the 1999.890 observations, with somewhat poorer u,v coverage, only when other epochs were unavailable. All plots shown here include just one epoch of each of the 177 sources. In the future it may be interesting to study variability in polarized intensity and polarization angle using those 66 sources with multiple epochs available, however no effort has been made toward this goal thus far.

Using optical classifications from the literature (Henstock et al. 1995; Vermeulen, Taylor, Readhead, & Browne 1996), from the NASA Extragalactic Database, and from unpublished observations by the CJ collaboration, we find that the final sample of 177 sources consists of 30 galaxies, 106 quasars, 20 BL Lacertae objects and 21 others, including empty fields, red and blue objects and other optically unresolved objects. We note here a few words of caution regarding the above classifications in that low-luminosity BL Lacs can be missidentified as quasars or radio galaxies (Marchã & Browne 1995), and variability in the emission lines of BL Lacs and quasars can cause some movement between these classes (Vermeulen et al. 1995). Redshifts have been measured for 147 of the sources presented here.

3. Observations

3.1. Calibration

The observations were carried out on 2000 December 16 and 17 (2000.958), 1999 November 21, 23 and 26 (1999.890), and 1998 February 8, 12, 13, 20 and 21 (1998.122). These three epochs provided about 34, 72 and 120 hours of data, respectively, for a total of 226 hours of observations. The 2000.958 and 1998.122 observations used the 10 element Very Long Baseline Array⁴ (VLBA) while the 1999.890 observations used only 8 of the VLBA antennas. The Saint Croix, Virgin Islands antenna was lost due to hurricane Lenny, and the North Liberty, Iowa antenna was lost due to a power hardware problem. Because we did not use phase referencing, we failed to image 6 sources with total intensity peaks of less than 55 mJy. Of these, four sources were identified with galaxies, and two sources had no optical identification. Another source, 0954+556, was omitted due to a position error of 30 arcseconds. Finally, the gravitationally lensed object 0218+357 was also omitted. These 8 sources that we did not image have not been included in any of the distributions or analysis, and are not included in the 177 source count.

We observed at 4995 MHz with a total bandwidth of 16 MHz. Right- and left-circular polarizations were recorded using 1 bit sampling at 64 Mbits/sec. Two intermediate frequencies (IFs) of 8 MHz each were used for right- and left- polarization. Amplitude calibration for each antenna was derived from measurements of the antenna gain and system temperatures during each run. Global fringe fitting was performed using the AIPS task FRING, an implementation of the Schwab & Cotton (1983) algorithm. The fringe fitting was performed on each IF and polarization independently using a solution interval of 2 minutes, and a point source model was assumed. Next, a short segment of the cross hand data from the strongly polarized calibrator 3C 279 was fringe fitted in order to determine the right-left delay difference, and the correction obtained was applied to the rest of the data. Once delay and rate solutions were applied the data were averaged in frequency over 8 MHz. All data were then averaged together over a 30 second time interval. Imaging, editing and self-calibration were performed in DIFMAP (Shepherd, Pearson & Taylor 1995) and AIPS.

Determination of the leakage terms was performed with the AIPS task LPCAL using a strong calibrator with simple source structure such as 0923+392 or 0716+714. Given the nature of the survey, strong sources with good parallactic angle coverage were abundant in every observing session. The absolute electric vector polarization angle (EVPA) calibra-

⁴The National Radio Astronomy Observatory is operated by Associated Universities, Inc., under cooperative agreement with the National Science Foundation.

tion was performed using various well-known target sources such as 0923+392, 1803+784, and 2200+420 (BL Lac). These observations were compared to contemporaneous short VLA observations and VLBI polarimetry reported in the literature, or available from the VLA/VLBA Polarization Calibration Page (Taylor & Myers 2000). We also used component C4 of 3C 279, which was fairly stable during this time period (Taylor 2000; Zavala & Taylor 2001). The absolute uncertainty in the EVPA calibration is $\sim 4^\circ$, with the dominant source of error being the variability of the EVPAs of the calibrator sources (Taylor & Myers 2000).

3.2. Data Analysis

We automated the imaging process by writing a script that ran the AIPS task IMAGR on the self-calibrated data for every source, creating Stokes I, Q and U maps. Using another script, we then ran the AIPS task COMB on each of the sources to produce polarized intensity maps, polarized intensity noise maps, polarization angle maps and polarization angle noise maps. Some sample images covering a range of morphologies are shown in Fig. 1. These FITS files were brought into IDL where we used programs to objectively and uniformly determine the properties of each source.

3.3. Source Property Definitions

The RMS noise levels were calculated for the total intensity and linear polarizations by taking the standard deviations of four corner sections of the image and averaging the two middle values. We calculated the integrated flux in Stokes I, Q and U by summing the flux in a particular region that completely enclosed each source. The algorithm used to systematically define the region boundaries creates a rectangular box around those pixels with values at least 15 times the RMS noise level. Due to image artifacts this high cut-off proved necessary to correctly enclose many sources. A border of width three times the FWHM of the convolving beam was added to the initial rectangular area to define the final region to be used in the summing. As a check we compared the integrated flux calculated in IDL to the sum of the clean components found in the AIPS task IMAGR. The total integrated flux measurements of all 177 sources were found to agree with that calculated by the AIPS clean algorithm to within 8%.

The core of each source was assumed to be located at the brightest peak in the total intensity map when no other data were available for study. However, in the case of compact

symmetric objects (CSOs) or sources with complex jet structures we took advantage of 15 GHz images (Taylor, Readhead & Pearson 1996) (and unpublished 15 GHz observations) and published motion studies (Taylor & Vermeulen 1997) to more accurately determine core positions. Jet component positions were found by subtracting from the initial total intensity image a Gaussian model centered at the peak flux position and scaled so that the maximum value of the Gaussian equaled the peak value in the map. As the appropriate Gaussian is subtracted from the previous image, the locations of each new peak define the locations of consecutive jet components. We add the restriction that the total intensity at the jet component position found must be greater than 9 times the RMS noise level, where the noise is calculated as discussed above. At most 8 jet component positions were required to describe a source. The position angle of the elliptical Gaussian model used in the subtraction was matched to the position angle of the convolving beam, and both axes of the Gaussian were given a width of 1.5σ , where $\sigma = \frac{FWHM}{2\sqrt{2\ln 2}}$ and describes the width of the convolving beam. Due to slight differences in the editing process that changed the u,v coverage for different Stokes parameters, the beam sizes and position angles fit by the AIPS task IMAGR differed slightly in I, Q and U. For consistency we forced all beams to have the dimensions and orientation of the Stokes U beam by setting the beam parameters BMAJ, BMIN and BPA in AIPS for the Stokes Q and I images.

The jet properties and source morphologies based on total intensities were easily characterized after each jet component position was defined. We found 34 sources with no jet components which we call *naked cores* and 134 sources with at least one jet component which we call *core-jet* sources. In addition, we found 9 sources which we classified as Compact Symmetric Objects (CSOs) or CSO candidates based on their symmetric structures. CSOs are a recently identified class of radio sources smaller than 1 kpc in size with emission on both sides of the central engine, and are thought to be very young objects (~ 1000 y, Readhead et al. (1996); Owsianik & Conway (1988)). Eight of these sources were previously identified as CSOs or CSO candidates (Peck & Taylor 2000), and the remaining source (0402+379) is currently under study.

We recorded the jet axis angle to be the angle defined by the core and the closest jet component, where North is 0° . The only exception to this is the CSO candidate 0402+379 which has a component close to the core but seemingly unrelated to the jet. The jet axis angle for this source was measured by eye. The jet length is defined in most cases as the distance from the core to the farthest jet component from the core, irrespective of jet bend. It is quoted in milliarcseconds and is uncorrected for angular distances. In §5 we model our angular size calculation after the description given in Kellermann (1993), creating a contour line at 2% of the peak in the total intensity map. The maximum distance from the contour line to the core position defines the angular size. To avoid measuring distances to spurious

peaks above the 2% level, we confined the contour to be within the same rectangular area that was previously determined to completely enclose the source.

We define integrated core flux densities as the pixel value at the core component, where the pixel values have units of Jy beam^{-1} and we assume the core itself to be unresolved. Due to complex jet structure, rather than sum the pixel values for the jet components we define the integrated jet flux as the difference between the integrated total source flux and the core flux.

Due to leakage between orthogonal polarization feeds in the antennas, we define *detected*, polarized cores or jet components as only those components in which the polarized intensity is greater than 0.2% of the peak in the total intensity image ($p > 0.002 I_{\text{peak}}$). We require detected polarizations to be above the 3σ level, where σ is described by the RMS noise in the Stokes Q and U maps by the relation $\sigma = (0.21 \sigma_U^2 + 0.21 \sigma_Q^2)^{1/2}$ according to Rayleigh statistics. In the case that the core has undetected polarization, we quote m_{core} as an upper limit equal to the larger of the two detection restrictions ($m_{\text{core}} \leq \max(0.002 I_{\text{peak}}, 3\sigma)$). When studying correlations between jet axis angle and polarization angle, we restrict our analysis to those components with $\sigma_\chi < 20^\circ$, where σ_χ is determined by the noise image created by the AIPS task COMB.

4. Results

Measured properties for each source are presented in Table 1. Additional information, including measured jet properties, is available on the world wide web⁵. Images are available upon request to the authors. Below we present a statistical analysis of source properties.

4.1. Core Fraction

From Fig. 2 it is clear that the core fractions of galaxies come from a different parent distribution than that of quasars or BL Lacertae objects. While quasars and BL Lacs generally exhibit a core fraction (defined $R_c = S_c/S_{\text{total}}$) $R_c \approx 80\%$, the 30 galaxies in our sample show no tendency toward either high or low core fraction. The tendency towards higher core fraction in quasar and BL Lacs is expected from unified schemes since the core fraction is a strong function of orientation. The Kolmogorov-Smirnov (K-S) test disproves the null hypothesis that the distribution of quasars (d_Q) and the distribution of BL Lacs

⁵www.aoc.nrao.edu/~gtaylor/cjftab.text

(d_{BL}) are the same as the distribution of galaxy core fractions (d_{G}). When comparing d_{Q} to d_{G} the K-S test outputs the maximum value of the absolute difference between the two cumulative distribution functions (c.d.f.'s), $D=0.45$ with a probability, p , that quasars and galaxies are drawn from the same population of 7.7×10^{-5} . Similarly, when comparing d_{BL} to d_{G} , we find a probability of 2.9×10^{-3} . Comparing d_{BL} to d_{Q} we find $p=0.41$, indicating that these samples could come from the same parent distribution. Since the cores and jets generally have different spectral indices, the core fraction will depend weakly on redshift. As an example, a source with $R_c = 0.75$ at a redshift of zero would shift to $R_c = 0.83$ at $z=1$ and $R_c = 0.87$ at $z=2$, assuming a flat spectrum core and steep ($\alpha = -0.7$) jets. In Fig. 2 we have not attempted any redshift correction so this could account for the minor difference between the shape of the distribution for the quasars and BL Lac objects.

The distribution of R_c in Fig. 2 for the galaxies appears somewhat bimodal. Of the 15 sources with $R_c < 0.5$ more than half (9/15) are CSOs. No obvious properties are identified with the high R_c population, although our knowledge of these sources is not complete.

One might be concerned that this comparison uses a sample of quasars four to five times as large as the samples of BL Lacs and radio galaxies, respectively. This should not be a factor if we consider the effective number of data points N_e as defined by Press et al. (1992). N_e is defined as

$$N_e = \frac{N_1 N_2}{N_1 + N_2} \quad (1)$$

where N_i are the number of data points in the respective sets. As long as N_e is greater than or equal to four the probability estimate should be accurate. For the quasar–galaxy comparison $N_e = 23.4$, quasar–BL Lac $N_e = 16.8$, and for BL Lac–galaxy $N_e = 12.0$.

4.2. Core and Jet Fractional Polarizations

Fig. 3 shows the distribution of average fractional polarization in the cores of quasars, galaxies and BL Lac objects. From this distribution we see that quasars have typical core polarizations of a few percent, and most (87%) are detected. Galaxies are clearly less polarized than quasars on the parsec scale with only 3 of 30 (10%) of the sources found to have detectable polarization in their cores. No detectable polarized flux was found from any of the 9 CSOs observed. This is consistent with results from a VLBI follow-up survey of CSOs by Peck & Taylor (2000) who found less than 1.2 mJy of polarized flux from each of 21 sources observed at 8.4 GHz with the VLBA. Generally we find less than 5 mJy of polarized

flux density and fractional polarizations of $<0.5\%$. For a few CSOs with weak cores, our upper limits on the fractional polarization are quite high. In contrast the BL Lacs appear to have slightly more strongly polarized cores than quasars (K-S test gives $p=0.20$ that they are drawn from the same population).

The K-S test only compares detections, and ignores the upper limits. Survival analysis (Feigelson & Nelson 1985) takes into account the upper limits in the comparison of two samples. Using the Penn State ASURV 1.2 package (Lavalley, Isobe, & Feigelson 1992) we tested the hypothesis that the BL Lac and quasar core fractional polarization results were drawn from the same parent distribution. Including the 15 upper limit quasar results decreased the likelihood that the two samples were drawn from the same parent distribution. The five two sample tests in ASURV 1.2 give an average probability of 1.5% that the null hypothesis is correct. This is significantly different from the K-S test result, and we find that this result is not affected by eliminating the one rather high upper limit quasar core fractional polarization of 2.7%.

Fig. 4 shows the same set of distributions, but for the average fractional polarizations of the jet components. In this case the fractional polarization of the BL Lacs is significantly greater from that of the quasars ($p=0.0037$ that they are drawn from the same population). When the jet polarization is detected, sources have higher fractional polarization in the jets than in the cores. Even the galaxies have an average fractional polarization in the jets of 10%, compared to typical fractional core polarizations of $<1\%$. In Fig. 5 we show the images for all six radio galaxies with some detected polarization. The measurements range from marginal in 0600+442 and 0847+379 to extremely detailed in the bright, one-sided jet of 1807+698.

4.3. Comparing Alignments Between Jet Axis and EVPA

Many claims have been made in the literature regarding comparisons of the orientation of the jet axis (θ) with the EVPA of the jet (χ_{jet}) or core (χ_{core}). Below we discuss various tests to look for preferred *alignments*. Ideally these tests should be made after having removed any Faraday rotation due to the ISM of our Galaxy, or the environment local to the sources. Unfortunately, for these single-frequency observations it was not possible to estimate the Rotation Measure (RM). If significant RMs exist towards any of the source components (e.g., as found to be common in quasar cores by Taylor 1998, 2000) then that will tend to smear out any intrinsic correlation.

The rotation measure of the cores of BL Lacs are typically 2–300 rad m^{-2} , and those

of quasars range from 200 rad m^{-2} to several 1000 rad m^{-2} (Zavala & Taylor 2003). At 5 GHz a rotation measure of 277 rad m^{-2} is enough to cause a turn of one radian. This would be sufficient to smear out any correlation in EVPA. The RMs in the jets of 16 BL Lacs, radio galaxies and quasars, with one exception, are all approximately 200 rad m^{-2} , and thus would also smear out any correlation in $\theta - \chi_{\text{jet}}$ (Zavala & Taylor 2003).

In Fig. 6 we present the distribution of $\theta - \chi_{\text{core}}$ for quasars, galaxies and BL Lac objects. For the quasars we see that the distribution is not quite flat, and hints at an excess of sources near 80 degrees. These nearly misaligned EVPAs imply a magnetic field nearly perpendicular to the jet axis assuming optically thick synchrotron emission. The K-S test indicates only a 0.3% chance that the distribution is the same as a flat distribution, suggesting the possibility of an intrinsic correlation between EVPA and θ . There is a somewhat greater probability (3.7%) that the quasars and BL Lacs are drawn from the same population. However, the BL Lac distribution itself is not significantly different from a flat distribution (17% chance that it is the same as flat).

To further investigate the nature of the misaligned core EVPAs we divided the quasars into those with short (length $< 6 \text{ mas}$) jets and long (length $> 6 \text{ mas}$) jets. From Fig. 7 we see that a jet length of 6 mas divides the quasars into two groups of roughly equal sizes since there are jet length peaks at 4 and 9 mas. We used ASURV’s correlation tests (Isobe, Feigelson, & Nelson 1986) to examine the correlation that appears in Fig. 8 for the quasars with short jets. Although it appears that short jets are correlated with misaligned core EVPAs, a Kendall’s tau test gives a less than 1 sigma significance of a correlation. Additionally, plots of $|\theta - \chi_{\text{core}}|$ versus jet length show no obvious correlation, regardless of jet length. Although there is no evidence for a correlation of quasar core EVPA alignment with jet length the K–S test of quasars versus a uniform distribution indicates that quasars have a preference for misaligned core EVPAs. As one can see from Fig. 8 the cores associated with short jets appear more misaligned (probability of a flat distribution is 0.009%, probability that they have the same distribution as sources with long jets is 1.7%), with a clear excess near 90 degrees. We also divided the quasars into those with a high ($R_c > 85\%$) or low ($R_c < 85\%$) core fraction. Core fraction seems much less important as a discriminator of the misaligned core EVPA population.

One can also look for any dependence on alignment with redshift. In Fig. 9 we plot the alignments of the jet and core EVPAs with jet axis against redshift. No trends with redshift are apparent for either the jets or the cores. Correlation tests performed using the ASURV package verified that no correlation of either core or jet misalignment with redshift is present. This was true for fractional polarization in the cores and jets as well.

In Fig. 10 we present the distribution of $\theta - \chi_{\text{jet}}$ for quasars, galaxies and BL Lac

objects for the jet components both near (< 6 mas) and far (> 6 mas) from the core. Contrary to claims in the literature (Cawthorne et al. 1993; Homan et al. 2002) that quasars have preferred alignments with the magnetic field oriented parallel to the jet axis, we see no such correlation. (The probability of being drawn from a flat distribution is 34%.) We have also tried examining separately the near (< 6 mas) and far (> 6 mas) jet components and reach the same conclusions. Cawthorne et al. did apply a rotation measure correction, which might reveal a correlation our non-RM corrected results hide. However, their RMs were derived from the VLA, which does not correctly sample the parsec-scale RM of these AGN. Additionally, the RM corrections were primarily (12/17) less than 50 rad m^{-2} , which amounts to a correction of 10° or less at 5 GHz. As shown in Zavala & Taylor (2003) these corrections were too small to account for the known parsec-scale RMs. Homan et al. did not apply a RM correction, but their observations were at 15 and 22 GHz. Their results are thus less susceptible to any rotation measure smearing.

The distribution for BL Lac objects (Fig. 10) appears to have a lack of sources with EVPA perpendicular to the jet. From the K-S test we find an 8.0% chance of this population being drawn from a uniform $\theta - \chi_{\text{jet}}$ distribution. A bimodal distribution was found by Gabuzda, Pushkarev & Cawthorne (2000) with peaks near 0° and 90° . Gabuzda et al. performed a similar analysis on a 1 Jy flux limited sample of BL Lac objects observed with VLBI polarimetry at 5 GHz. This is shown in Fig. 12 of Gabuzda, Pushkarev & Cawthorne (2000). A K-S test of the data in their Fig. 12 yields a 1.1% probability that the data are drawn from a uniform distribution. With assistance from Gabuzda (2002, private communication) we combined our BL Lac $\theta - \chi_{\text{jet}}$ data with the 35 measurements from Gabuzda, Pushkarev & Cawthorne (2000) and tested this data against a uniform distribution in a K-S test. The combination of these two samples results in a 0.7% probability that the parent distribution is uniform. However, with just the 17 data points from our sample it is difficult to draw a conclusion on the nature of the underlying distribution, and we cannot hope to isolate what type of source gives rise to the slight excess of sources with EVPA at small angles to the jet axis.

In a 43 GHz polarimetry survey of flat-spectrum sources from the Pearson-Readhead survey (Pearson & Readhead 1988), Lister (2001) found that the most strongly polarized quasar cores display EVPAs that are aligned with the jet axis. In Fig. 11 we examine the relationship between alignment and fractional polarization. No preferred alignment for the more polarized sources, as what Lister (2001) found, is evident in our sample. Also the preferred core EVPA orientation in our sample is for EVPAs perpendicular to the jet (Fig. 6). These two claims can be reconciled with the same projected magnetic field orientation if the cores are optically thin at 43 GHz and optically thick at 5 GHz.

Using the ASURV bivariate tests (Isobe, Feigelson, & Nelson 1986) we examined the hypothesis that there is a correlation between the core fractional polarization and the core EVPA alignment. The Kendall’s tau test gives a probability of 82.7% and the Cox regression a probability of 96.9% that a correlation does not exist. Although there appears to be a slight excess of sources with misaligned core EVPAs at fractional polarizations greater than 2.5%, this is not born out by the bivariate tests. The Cox regression gives a probability of 94.7% and the Kendall’s tau test a 43.6% probability that no correlation is present. The disparity probably results from small number statistics as only 20 sources have $m_{\text{core}} > 2.5\%$.

4.4. Fractional Polarization and Jet Length

In Fig. 12 the core and average jet fractional polarization is plotted against the projected jet length. The fractional jet polarization seems fairly smoothly distributed, but the fractional core polarization is anti-correlated with jet length. Sources with short jets seem to have higher core polarizations and there is a distinct lack of strongly polarized cores in sources with long jets. The censoring present in the lower panel of Fig. 12 led us to use survival analysis to test for a correlation for core EVPA alignment with jet length. Both the Kendall’s tau and Spearman’s rho tests give a weak (1.6σ) support to the anti-correlation which seems to be present. A possible explanation for this trend is that sources with long jets are viewed at angles farther from the line-of-sight. Assuming the standard obscuring torus model, the angle to the core then traverses a higher-density region with magnetic fields causing Faraday depolarization. This interpretation is also consistent with the finding that the cores of BL Lacs (thought to be viewed at very small angles to the line-of-sight (Antonucci 1993)) are somewhat more strongly polarized than quasar cores.

5. Cosmology Using the Size–Redshift Relation

The $\theta - z$ relation for compact radio sources has been studied in the past to place limits on q_0 . Kellermann (1993) used a sample of 82 core-jet sources selected from the literature to find that the deceleration parameter is roughly 0.5, without appealing to source evolution. Gurvits, Kellermann, & Frey (1999) did a similar analysis using 330 5 GHz compact sources taken from the literature, finding that $q_0 = 0.21 \pm 0.30$ if no linear size–luminosity, –redshift or –spectral index dependences are assumed. Gurvits, Kellermann, & Frey (1999) applied a regression model to 145 of the 330 sources with additional restrictions on luminosity and spectral index. With this subset of sources a deceleration parameter of $q_0 = 0.33 \pm 0.11$ was found. All of these results are consistent with Friedmann cosmologies with $0 \leq q_0 \leq 0.5$ and

$\Lambda=0$.

Figure 13 shows the θ – z relationship for 103 core-jet sources from our complete sample and mirrors Fig. 1 in Kellermann (1993) and Fig. 5 in Gurvits, Kellermann, & Frey (1999). We measured angular sizes similarly to how Kellermann and Gurvits did, accounting for the decrease in brightness with redshift as described in § 3.3. CSOs have been excluded due to the proposed relation between their age and angular size, and BL Lacertae objects have been excluded because of their proposed preferred inclination angles and to be consistent with the methods of Kellermann (1993). The redshifts range from $0.0172 \leq z \leq 3.469$. With the exception of the slope between the first two redshift bins, our plot shows no clear dependence between angular size and redshift. Binning the data in redshift space rather than restricting each bin to equal numbers of sources does not greatly alter the plot. We found that plotting median values rather than mean values also does not change the plot’s shape considerably. Thus contrary to previous claims our complete, flux-density limited sample, although not inconsistent with Friedmann cosmologies, cannot definitively rule out a steady state universe or place any limits on q_0 . The few sources with higher angular sizes and reasonable error bars clustered around $z=1.1$ are, however, suggestive of a general increase of angular size with redshift after $z=1$, which supports inflationary cosmologies.

Although these compact radio sources with smaller redshifts and younger ages are not as subject to evolutionary effects, and although the physical parameters of their central engines are thought to outweigh any effects due to possible variations of intergalactic medium with redshift, we find that these objects nevertheless cannot be used to place restrictions on the deceleration parameter and the geometry of our universe. The large error bars in Fig. 13 prove these sources to be poor standard rods, possibly because of their rapid evolution compared to the Hubble time. It is possible that strong Doppler favoritism is skewing our results so that more objects with small inclinations to the line-of-sight and therefore greater, Doppler-boosted luminosities and smaller angular sizes are getting into the sample without being excluded by the flux density requirement. Our neglect of Doppler boosting may also affect our measurement of angular size since we have defined object size by the contour line at 2% of the peak in the total intensity map. Angular size might also be better measured taking into account jet bend, rather than assuming a one-dimensional jet in all cases. Lastly, it is possible that with a multi-frequency study using an angular size–spectral index relation, as is shown in Fig. 7 of Gurvits, Kellermann, & Frey (1999), the θ – z correlation may become tighter.

5.1. Bent-Jet Sources and Other Interesting Properties

Although we did not do an exhaustive statistical analysis of the correlation between jet bending and other source properties, we do note two basic categories into which most bent sources fall. One class of bent jets typically shows little or no polarized intensity in the jet, while there may be polarized intensity at the source core. Some examples of this are 0600+442, 0700+470, 0707+476, 0831+557, and 0843+575. The second and larger class of bent jets shows a tendency for the electric field to follow the curve of the bending axis so that the electric vector position angles are usually, but not always, perpendicular to the bending axis of the jet. Figure 14 shows 0133+479, 0627+532, 1151+408, 1459+480, 1619+491, and 2351+456 which are all typical sources in this second category. A nice example of an \mathbf{E} -field bending with and parallel to the jet axis is the quasar 0627+532.

6. Conclusions and Future Work

A new, fairly strong correlation between core EVPA and jet axis angle has been discovered in quasars with projected jet lengths shorter than 6 mas. These objects exhibit \mathbf{E} -fields nearly perpendicular to the axis while those quasars with jet lengths longer than 6 mas show no obvious $\theta - \chi_{\text{core}}$ correlation. That this correlation exists in spite of the tendency of quasar cores to have substantial Faraday RMs (Taylor 1998, 2000), implies that the actual correlation is even stronger than we observe. These findings suggest that quasars with axes anti-aligned with the \mathbf{E} -field are not intrinsically different from those without this correlation; rather, the long-jet sources may be at larger angles to the line-of-sight so that the angle to the core traverses a higher-density region with magnetic fields that produce sufficient Faraday rotation to smear out any intrinsic correlation. This reasoning also can explain the sparsely populated region of high projected jet lengths and high fractional core polarizations in Fig. 12. These results can be made consistent with the finding of Lister (2001), of electric vectors aligned with the jet axis at 43 GHz if the cores are optically thick at 5 GHz, but optically thin at 43 GHz. A magnetic field perpendicular to the jet direction could be produced by a strong transverse shock (e.g. Laing 1980).

Unlike the preferred alignment found in quasar cores and contrary to previous claims in the literature (Cawthorne et al. 1993; Homan et al. 2002), quasar jets are not found to exhibit a $\theta - \chi$ relationship. This seems to be the case regardless of jet length, core dominance, or fractional polarization.

In contrast to quasar cores, BL Lac cores in our sample show no strongly preferred alignment. Since BL Lacs are observed to have lower Faraday Rotation Measures than

quasars (Zavala & Taylor 2003), it is unlikely that the absence of correlation is due to Faraday rotation. BL Lacs may be intrinsically different from quasars (i.e., have a lower power), or their intrinsic high variability may make it impossible to find a correlation over just one epoch, with only a modest number of sources (17). Future multi-epoch analysis, and/or the analysis of a larger sample, is necessary to conclusively determine the existence of any preferred alignment. An interesting test to make in the future would be to use spectral information to look for preferential alignments in optically thick or thin cores. Contrary to claims made by Gabuzda, Pushkarev & Cawthorne (2000) of a bimodal $\theta - \chi_{\text{jet}}$ distribution, the EVPA in BL Lac jets similarly show no correlation with the jet axis angle.

We found no evolution of source properties (size, fractional polarization, or polarization angle) with redshift. This lack of evolution is reasonable if the physical parameters of the central engine outweigh any effects due to possible variations of intergalactic medium with redshift.

We thank Rene Vermeulen and Silke Britzen for help in scheduling and for sharing the data. LKP thanks NSF for summer support through the Research Experience for Undergraduates (REU) program. We thank Travis Rector and Denise Gabuzda for helpful discussions. We also thank an anonymous referee for numerous helpful suggestions. This research has made use of the NASA/IPAC Extragalactic Database (NED) which is operated by the Jet Propulsion Laboratory, California Institute of Technology, under contract with the National Aeronautics and Space Administration.

REFERENCES

- Antonucci, R. 1993, *ARA&A*, 31, 473
- Britzen, S., Vermeulen, R. C., Taylor, G. B., Readhead, C. S., Pearson, T. J., Henstock, D. R., & Wilkinson, P. N. 22-26 June, 1998, in BL Lac Phenomenon conference held in Turku, Finland, p. 431
- Cao, X. & Jiang, D. R. 2002, *MNRAS*, 331, 111
- Cawthorne, T. V., Wardle, J. F. C., Roberts, D. H., Gabuzda, D. C., & Brown, L. F. 1993, *ApJ*, 416, 519
- Feigelson, E. D. & Nelson, P. I. 1985, *ApJ*, 293, 192
- Gabuzda, D.C., Pushkarev, A.B., & Cawthorne, T.V. 2000, *MNRAS*, 319, 1109
- Gabuzda, D.C. 2002, Bologna Jets Workshop, in press Pushkarev, A.B., & Cawthorne, T.V. 2000, *MNRAS*, 319, 1109
- Gómez, J. L., Marscher, A. P., Alberdi, A., Jorstad, S. G., & García-Miró, C. 2000, *Science*, 289, 2317
- Gurvits, L. I., Kellermann, K. I., & Frey, S. 1999, *A&A*, 342, 378
- Henstock, D. R., Browne, I. W. A., Wilkinson, P. N., Taylor, G. B., Vermeulen, R. C., Pearson, T. J., & Readhead, A. C. S. 1995, *ApJS*, 100, 1
- Homan, D. C., Ojha, R., Wardle, J. F. C., Roberts, D. H., Aller, M. F., Aller, H. D., & Hughes, P. A. 2002, *ApJ*, 568, 99
- Isobe, T., Feigelson, E. D., & Nelson, P. I. 1986, *ApJ*, 306, 490
- Kellermann, K. I. 1993, *Nature*, 361, 134
- Lavalley, M., Isobe, T., & Feigelson, E. 1992, *Astronomical Data Analysis Software and Systems I*, A.S.P. Conference Series, Vol. 25, 1992, Diana M. Worrall, Chris Biemesderfer, and Jeannette Barnes, eds., p. 245., 1, 245
- Laing, R. A. 1980, *MNRAS*, 193, 439
- Lister, M. L. & Marscher, A. P. 1997, *ApJ*, 476, 572
- Lister, M. L. 2001, *ApJ*, 562, 208

- Marchã, M. J. M. 1995, MNRAS, 275, 951
- Meier, D. L., Koide, S., & Uchida, Y. 2001, Science, 291, 84
- Owsianik, I., & Conway, J. E. 1998, A&A, 337, 69
- Roberts, D. H., Potash, R. I., Wardle, J. F. C., Rogers, A. E. E., & Burke, B. F. 1984, IAU Symp. 110: VLBI and Compact Radio Sources, 110, 35
- Roberts, D. H., Brown, L. F., & Wardle, J. F. C. 1991, ASP Conf. Ser. 19: IAU Colloq. 131: Radio Interferometry. Theory, Techniques, and Applications, 281
- Pearson, T. J., & Readhead, A. C. S. 1988, ApJ, 328, 114
- Peck, A. B., & Taylor, G. B. 2000, ApJ, 533, 95
- Polatidis, A. G., Wilkinson, P. N., Xu, W., Readhead, A. C. S., Pearson, T. J., Taylor, G. B., & Vermeulen, R. C. 1995, ApJS, 98, 1
- Press, W. H., Teukolsky, S. A., Vetterling, W. T., & Flannery, B. P. 1992, Numerical Recipes in C: The Art of Scientific Computing (2nd ed.; Cambridge: Cambridge University Press)
- Readhead, A. C. S., Taylor, G. B., Xu, W., Pearson, T. J., Wilkinson, P. N., & Polatidis, A. G. 1996, ApJ, 460, 612
- Schwab, F. R., & Cotton, W. D. 1983, AJ, 88, 688
- Shepherd, M. C., Pearson, T. J., & Taylor, G. B. 1994, BAAS, 26, 987
- Taylor, G. B., Vermeulen, R. C., Pearson, T. J., Readhead, A. C. S., Henstock, D. R., Browne, I. W. A., & Wilkinson, P. N. 1994, ApJS, 95, 345
- Taylor, G. B., Readhead, A. C. S., & Pearson, T. J. 1996, ApJ, 463, 95
- Taylor, G. B., Vermuelen, R. C., Readhead, A. C. S., Pearson, T. J., Henstock, D. R., & Wilkinson, P. N. 1996, ApJS, 107, 37
- Taylor, G. B., Vermeulen, R. C. 1997, ApJ, 485, L9
- Taylor, G. B. 1998, ApJ, 506, 637
- Taylor, G. B. 2000, ApJ, 533, 95

Taylor, G. B. & Myers, S. T. 2000 VLBA Scientific Memo 26, National Radio Astronomy Observatory

Wilkinson, P. N. et al. 2001, *Physical Review Letters*, 86, 584

Vermeulen, R. C., Ogle, P. M., Tran, H. D., Browne, I. W. A., Cohen, M. H., Readhead, A. C. S., Taylor, G. B., & Goodrich, R. W. 1995, *ApJ*, 452, L5

Vermeulen, R. C., Taylor, G. B., Readhead, A. C. S., & Browne, I. W. A. 1996, *AJ*, 111, 1013

Zavala, R. T. & Taylor, G. B. 2001, *ApJ*, 550, L147

Zavala, R. T. & Taylor, G. B. 2003, *ApJ*, in press

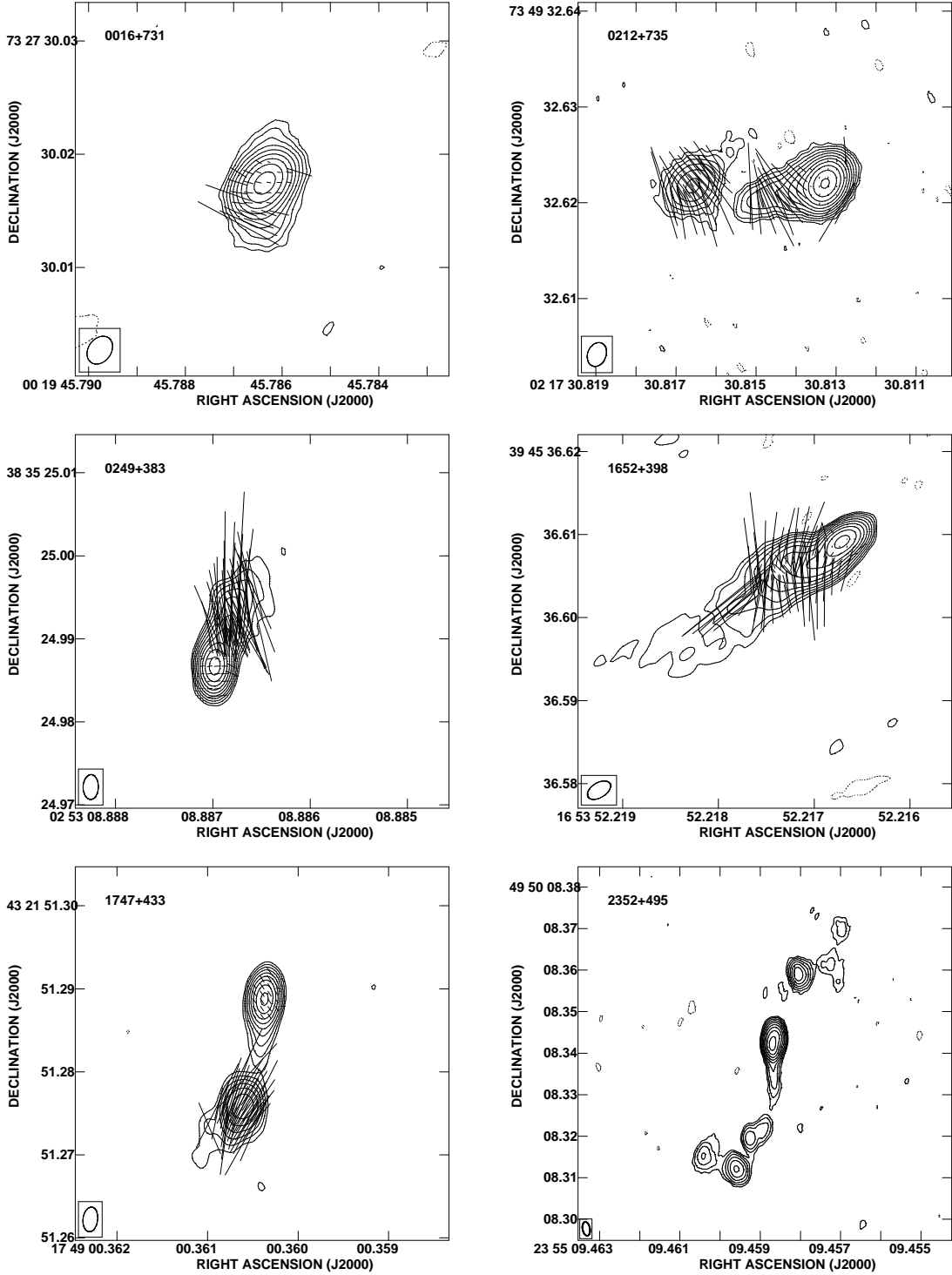


Fig. 1.— A selection of images from the sample showing a range of core-jet morphologies and the CSO 2352+495. Contours are drawn at $-4\sigma_I$, $4\sigma_I$, $8\sigma_I$, $16\sigma_I$, ..., where σ_I is RMS of total intensity given in Table 1. Polarization vectors have lengths proportional to fractional polarization. Blanking of the polarization has been performed on pixels less than $4.6\sigma_p$ in polarization, $9\sigma_I$ in total intensity, or 0.2% in fractional polarization.

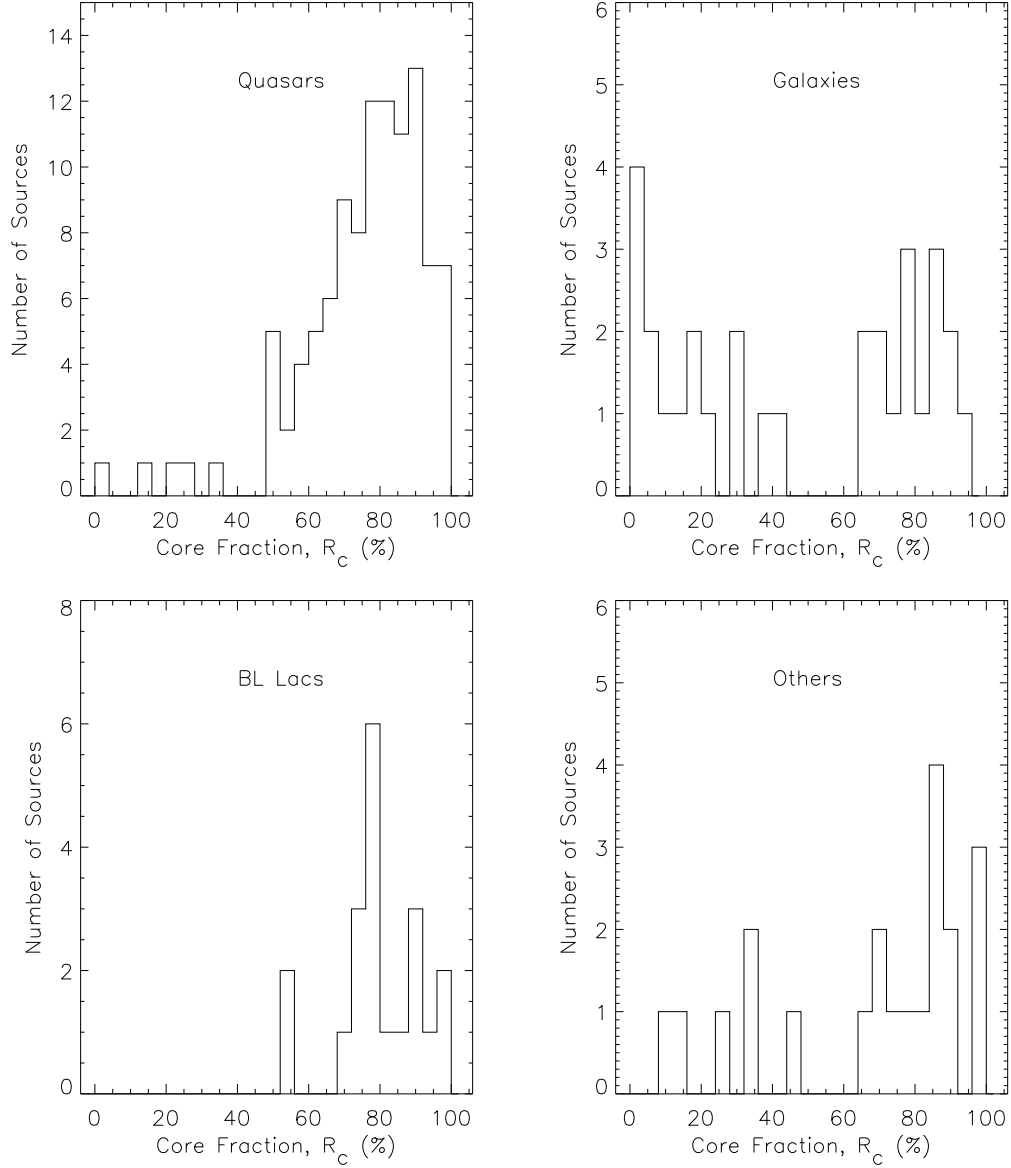


Fig. 2.— Distribution of core fractions, R_c , in quasars, galaxies, BL Lacertae objects and others, given as a percentage. R_c is the Stokes I flux density in the core divided by the integrated Stokes I flux density in the source, where we have calculated the core flux as described in § 3.3. The width of each bin is 4%. All sources are shown.

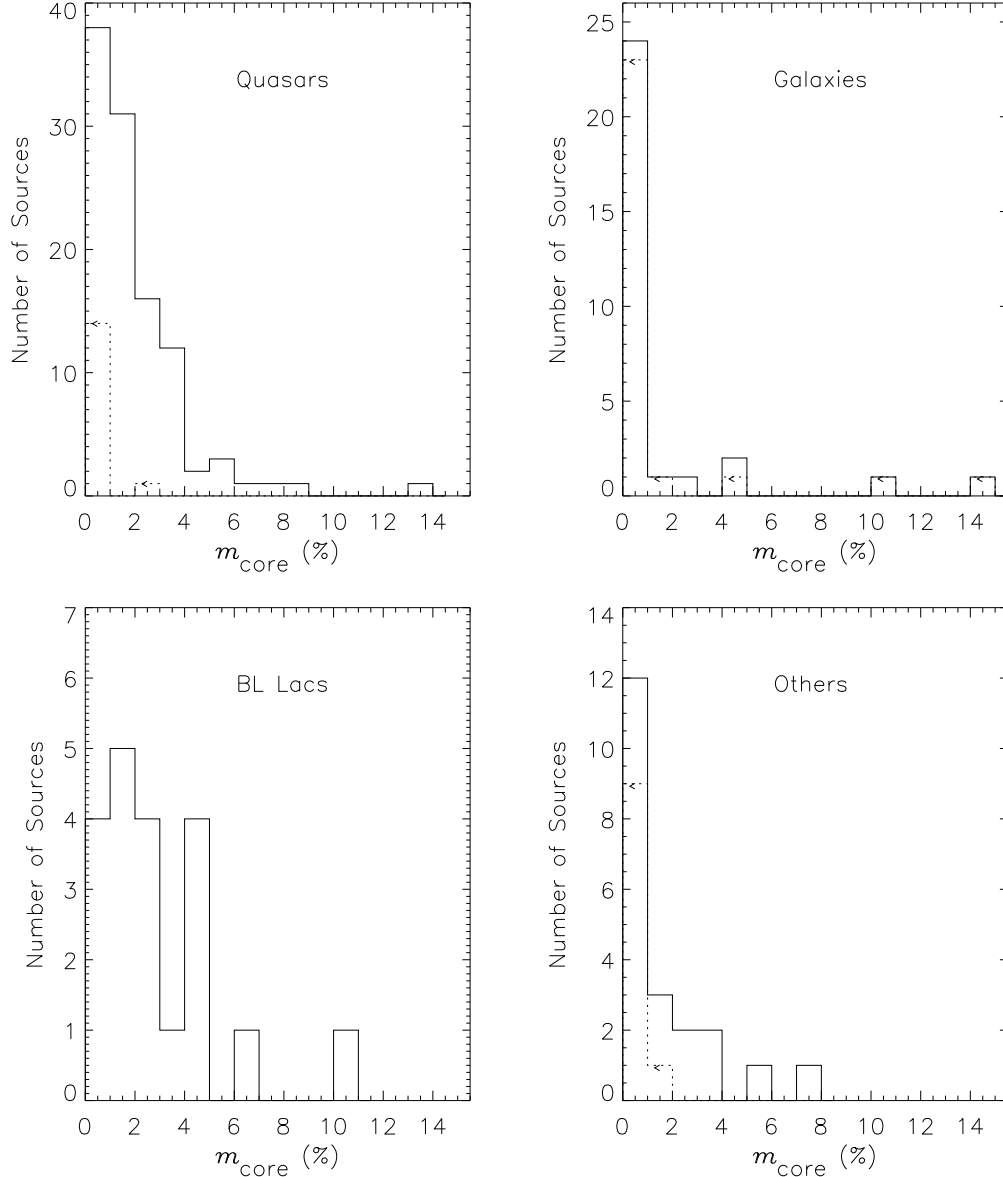


Fig. 3.— Distribution of the fractional polarization (m) in the cores of quasars, galaxies, BL Lacertae objects, and others, given as a percentage. Upper limits are shown as dashed lines with the < symbol. The solid line represents the sum of the upper limits and detections in each bin. Upper limits were assumed when the polarized intensity $p < 0.2\%$ of the peak in the total intensity image, or when $p < 3\sigma$, where σ is the RMS noise calculated as described in § 3.3. The quasar distribution represents 106 sources with 15 upper limits. The galaxy distribution represents 30 sources with 27 upper limits. The BL Lacertae distribution represents 20 sources with no upper limits, and the distribution of other sources represents 21 sources with 10 upper limits. The width of each bin is 1%.

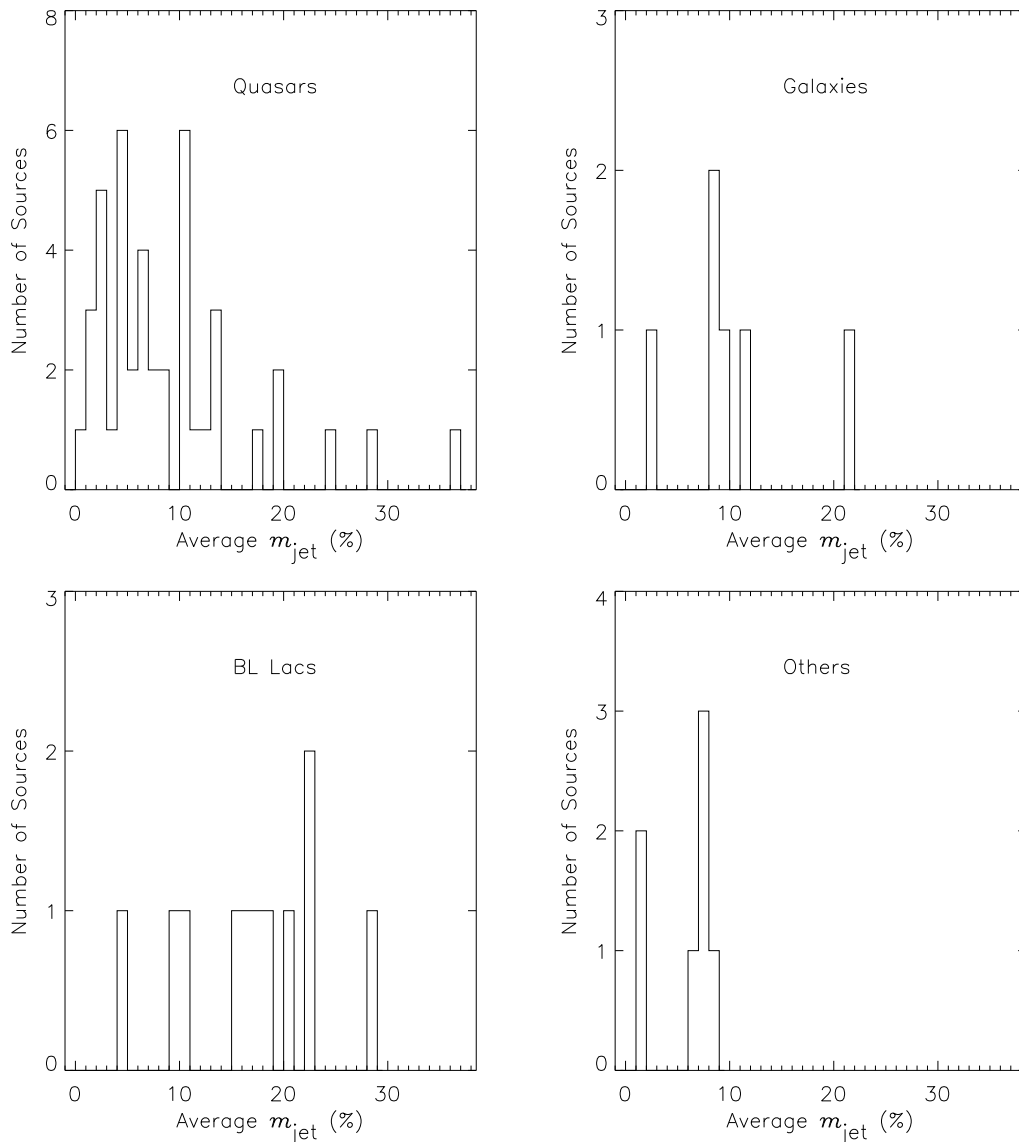


Fig. 4.— Distribution of the average fractional polarization (m) in the jets of quasars, galaxies, BL Lacertae objects, and others, given as a percentage. Only detected jet components have been averaged. (See § 3.3 for a definition of detected components.) The distribution of quasars represents 43 of the 106 we have in our sample. 21 quasars were excluded due to their naked core morphology, and 42 sources had no jet components with detected polarizations. The distribution of galaxies represents 6 sources. Four were excluded as they were naked cores, and 20 had no detected jet components. The distribution of BL Lacertae objects represents 11 sources. Three BL Lacs were naked cores and 6 had no detected jet components. The distribution of others represents 7 sources. 6 were naked cores and 8 had undetected jet components. The width of each bin is 1%.

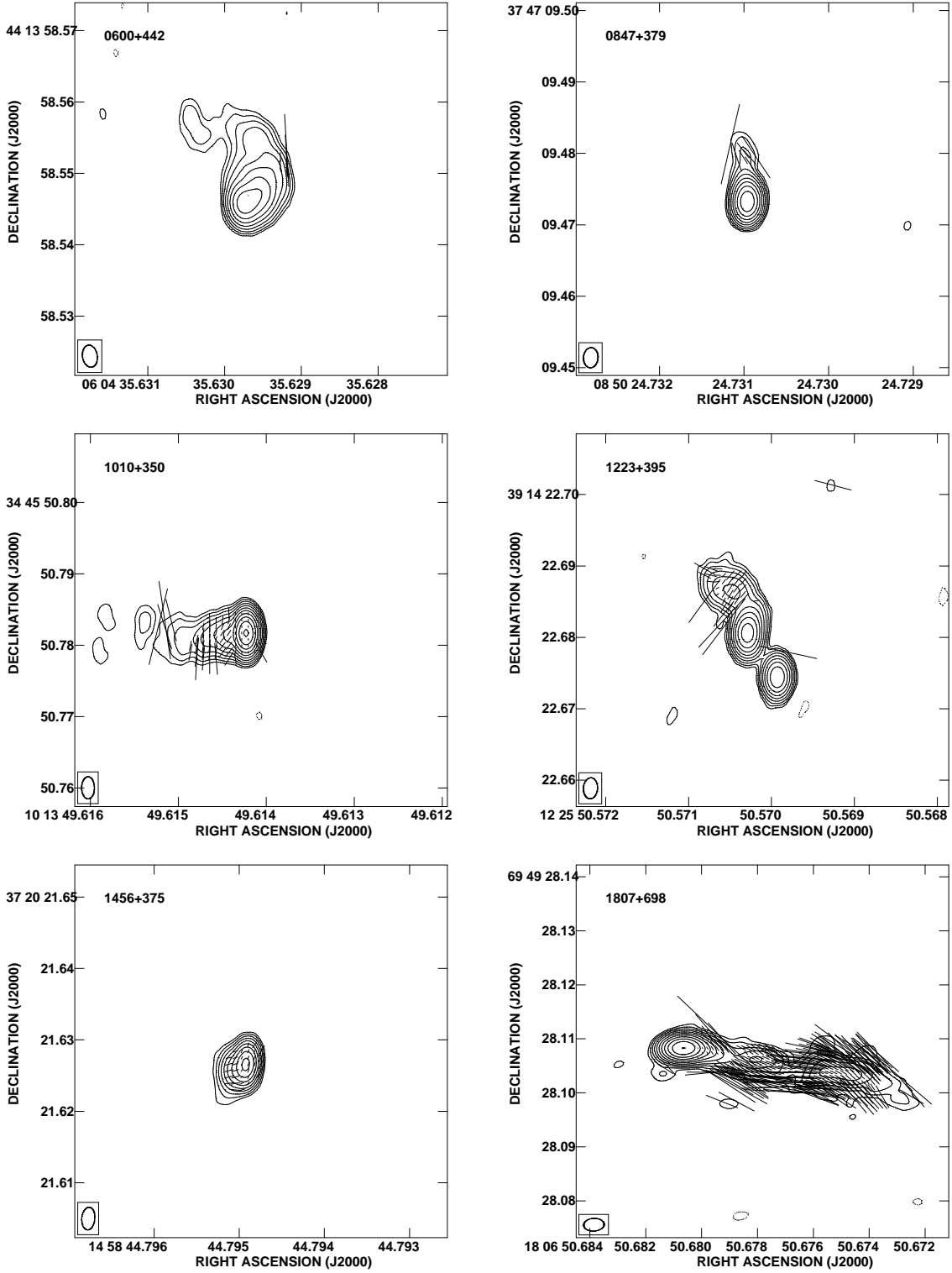


Fig. 5.— A plot of all six radio galaxies within our sample having some detected polarization. Contours are drawn at $-4\sigma_I$, $4\sigma_I$, $8\sigma_I$, $16\sigma_I$, ..., where σ_I is RMS of total intensity given in Table 1. Polarization vectors have lengths proportional to fractional polarization. Blanking of the polarization has been performed on pixels less than $3\sigma_p$ in polarization, $4\sigma_I$ in total intensity, or 0.2% in fractional polarization.

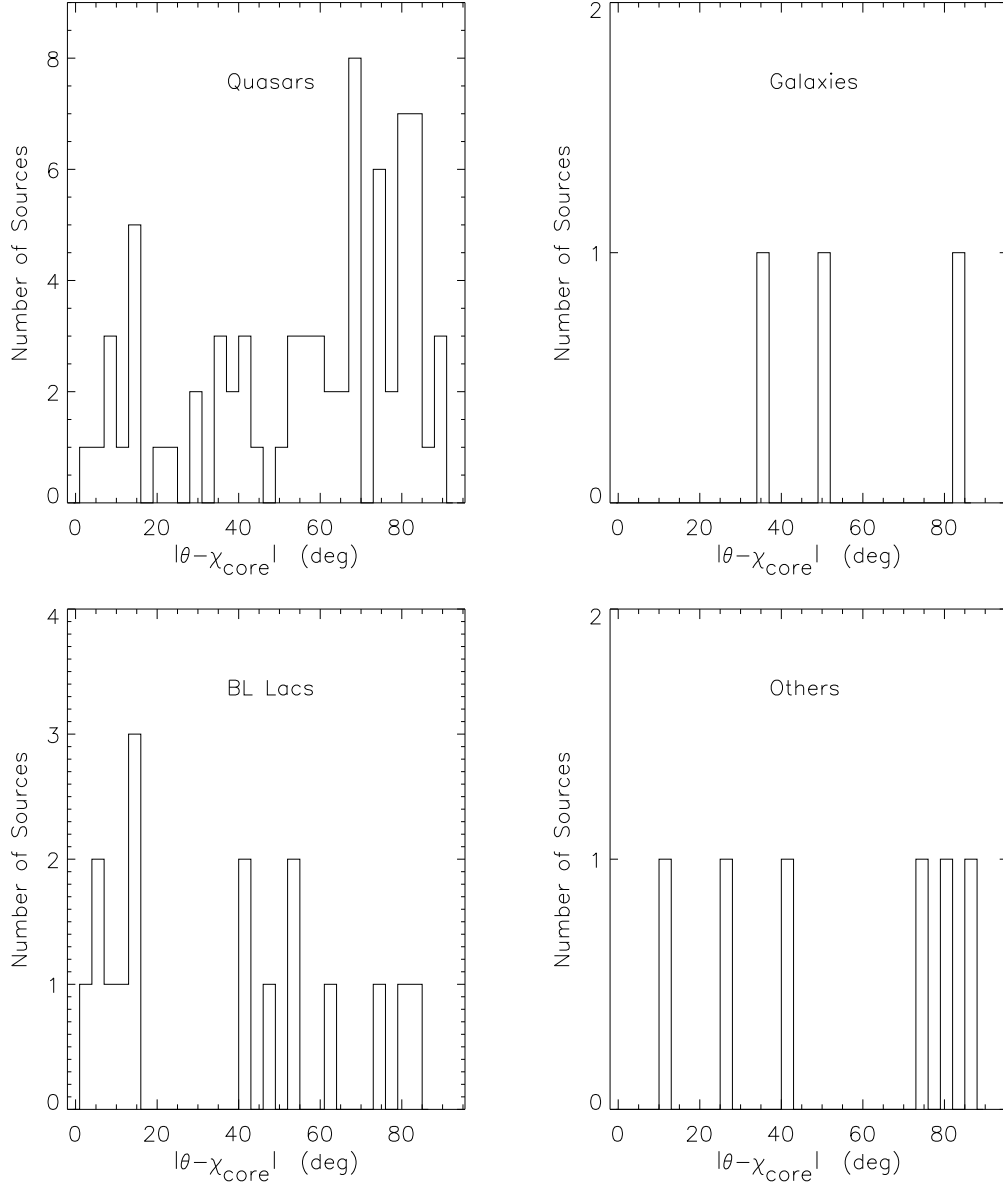


Fig. 6.— Distribution of the difference between the jet axis angle, θ , and the electric vector position angle at the core, χ_{core} given in degrees. The distribution of quasars represents 72 sources. 21 quasars were excluded due to their naked core morphologies, and 13 were excluded as they did not meet the detection criteria described in § 3.3. The distribution of galaxies represents just 3 sources, where 4 galaxies were found to have naked core morphologies and 23 had undetected cores. 17 BL Lacertae objects are shown. Three naked core BL Lacs were excluded. The distribution of others represents 6 sources. 9 had undetected core polarizations, and 6 were naked cores. The width of each bin is 3° .

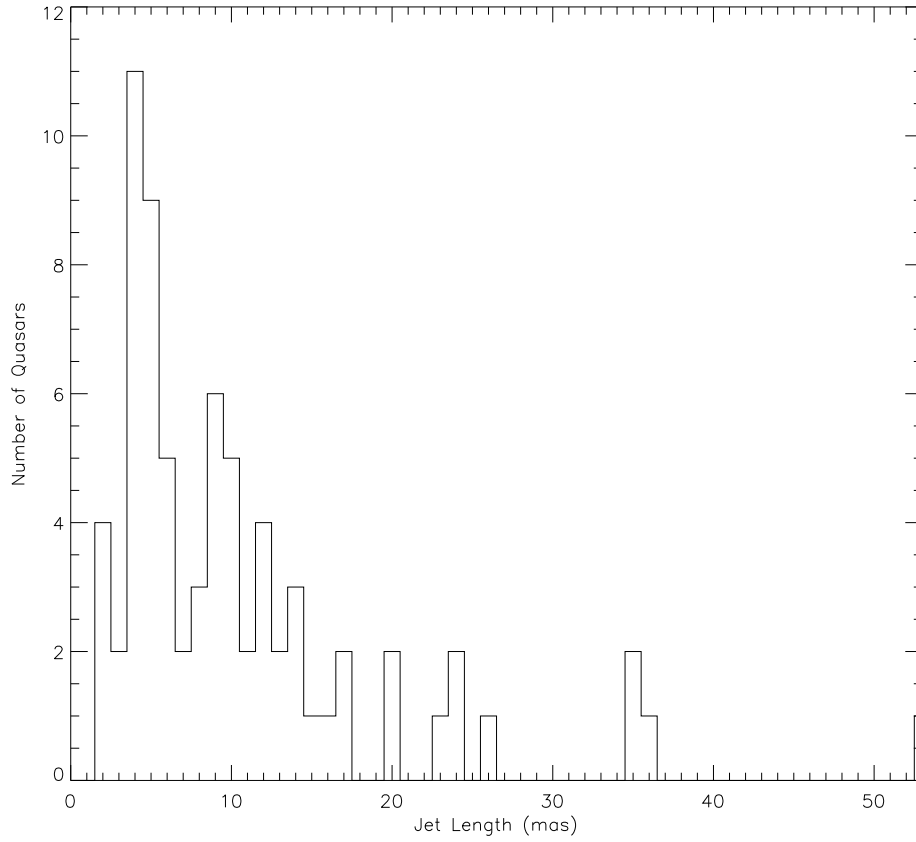


Fig. 7.— Distribution of uncorrected jet lengths for the 72 quasars shown in Fig. 6. The width of each bin is 1 mas.

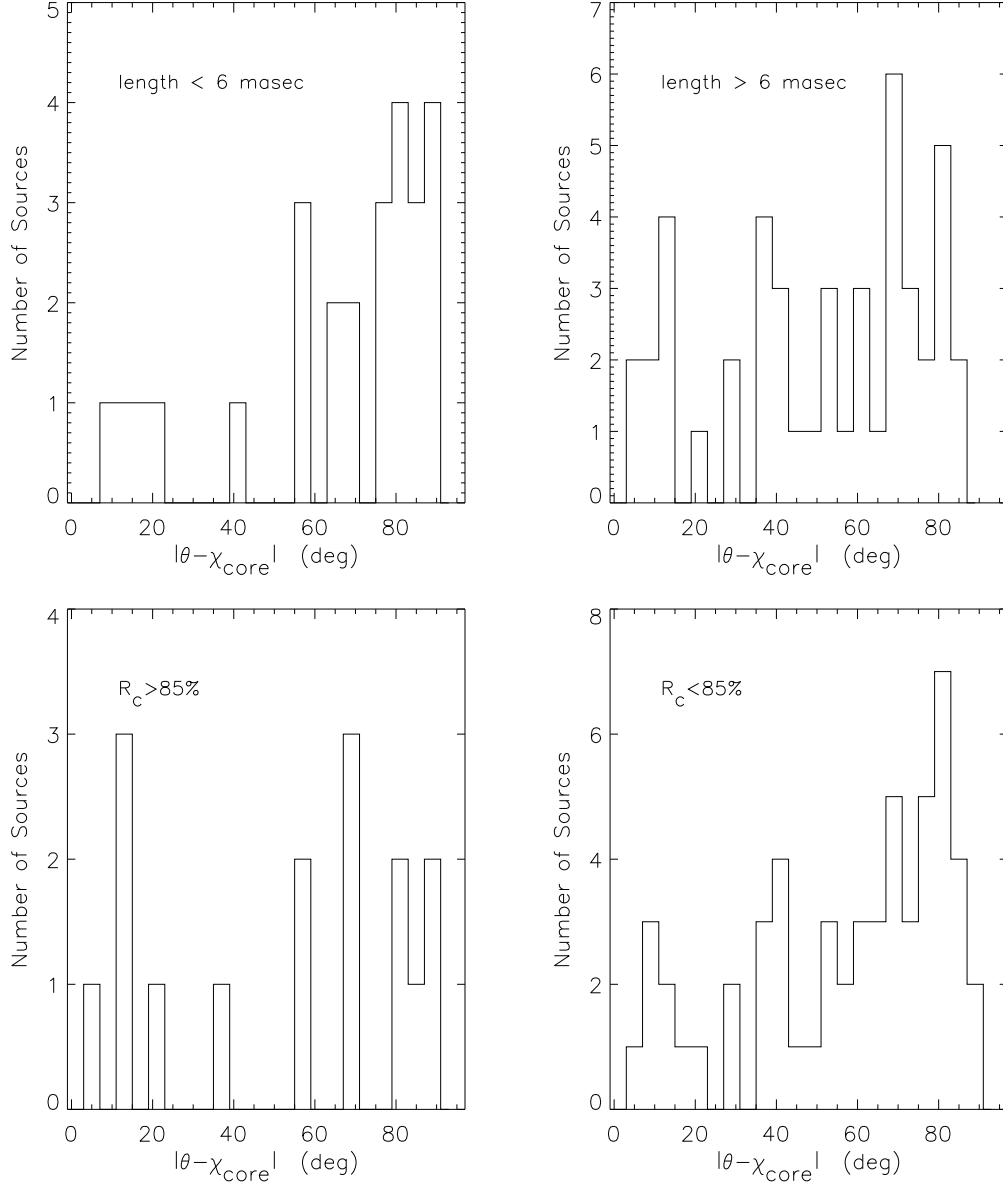


Fig. 8.— Distribution of the difference between the jet axis angle, θ , and the electric vector position angle at the core, χ_{core} , for quasars. Top left: $\theta - \chi_{\text{core}}$ relation for those quasars with uncorrected lengths of less than 6 mas. 26 quasars are shown. Top right: relation for quasars with lengths greater than 6 mas. 46 quasars are shown. Bottom left: $\theta - \chi_{\text{core}}$ relation for those quasars with core fractions greater than 0.85. 16 quasars are shown. Bottom right: relation for quasars with core fractions less than 0.85. 56 quasars are shown. Here we measure length as the angular distance from the core to the farthest jet component, irrespective of jet bend. The width of each bin is 4°.

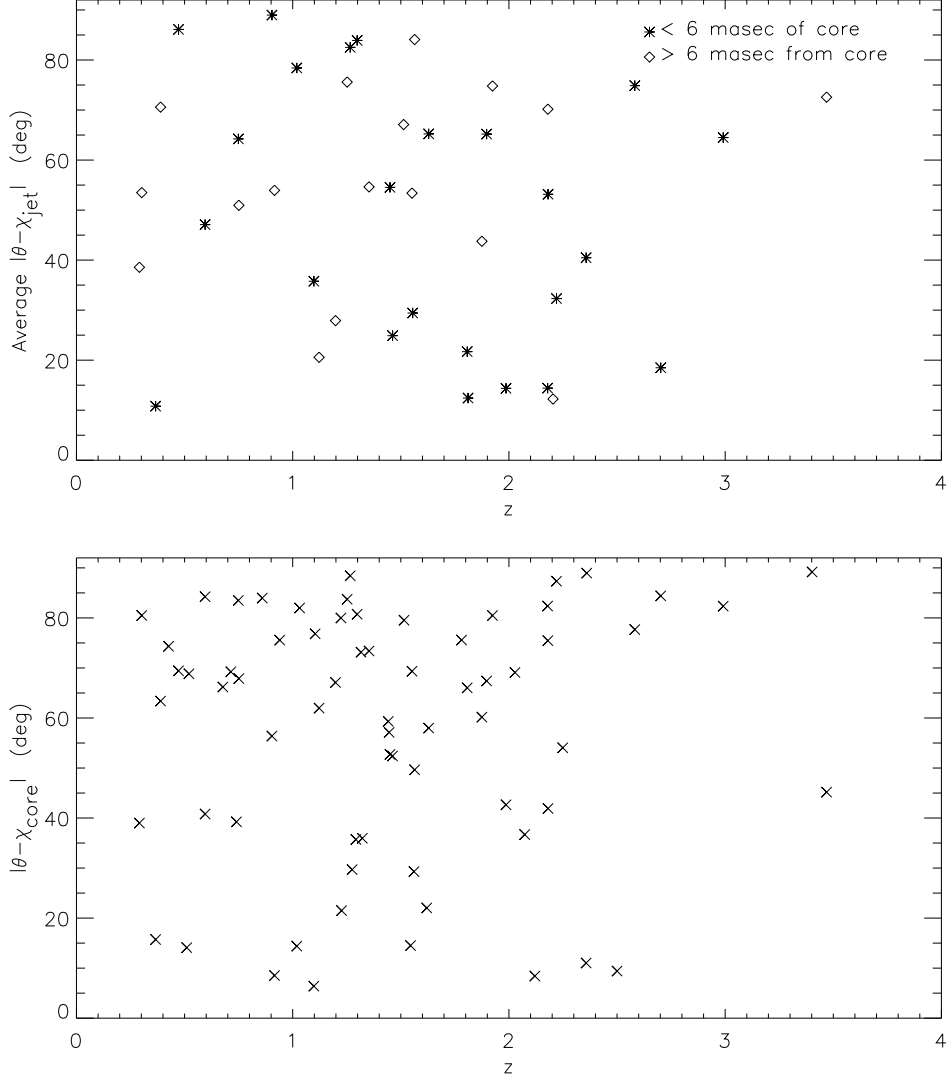


Fig. 9.— Top: Plot of the average difference between the jet axis angle, θ , and the electric vector position angle in the detected jet components of quasars, χ_{jet} , as a function of redshift. We have averaged the jet components within 6 mas of the core separately from those farther than 6 mas from the core, so that any quasar with detected jet components both farther and nearer than 6 mas from the core is represented twice. 24 quasars with detected jet components within 6 mas of the core are shown, and 17 quasars with detected jet components farther than 6 mas of the core are shown. Bottom: Plot of $|\theta - \chi_{\text{core}}|$ for those quasars with detected core polarizations as a function of redshift. 68 quasars are shown.

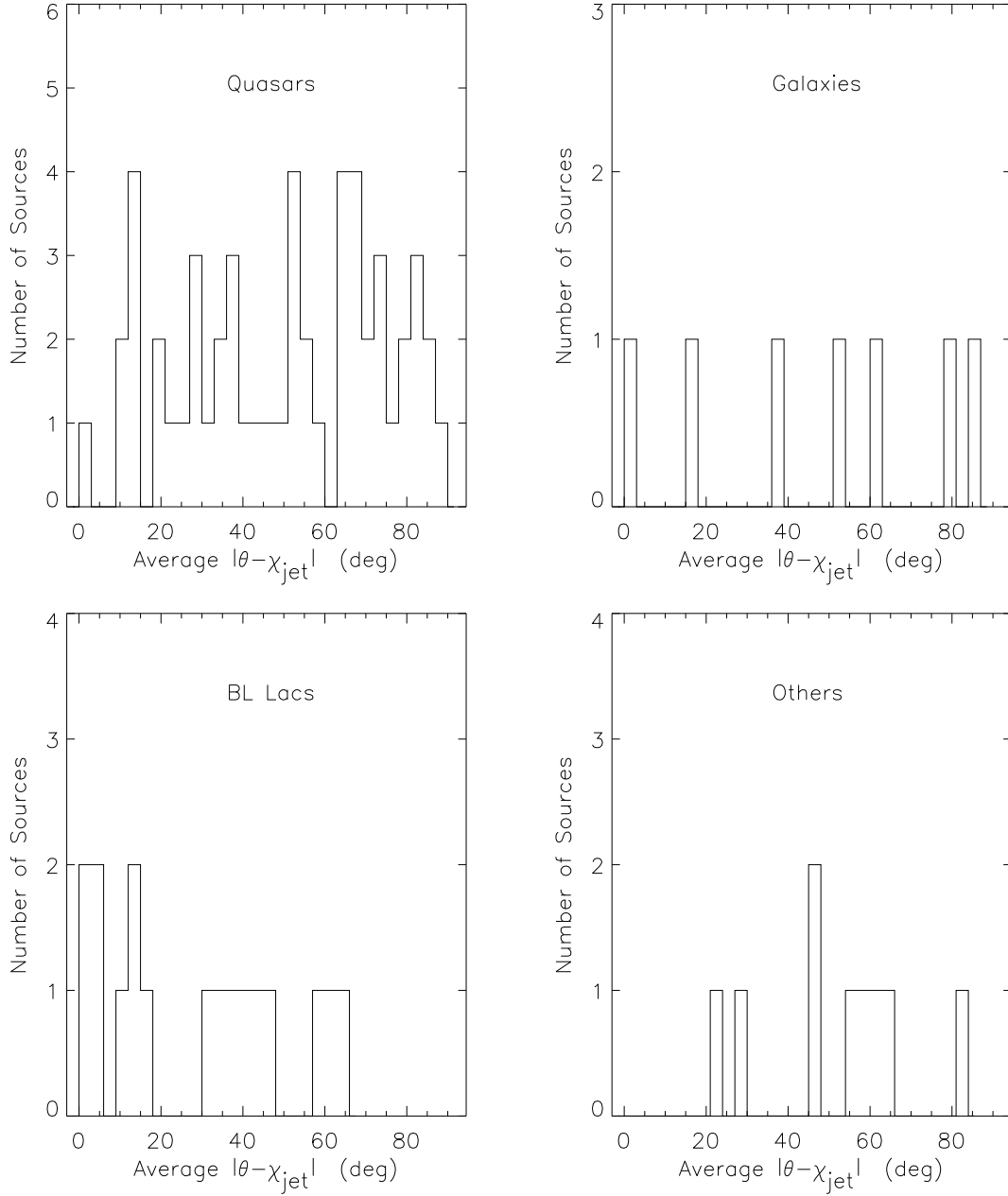


Fig. 10.— Distribution of the average difference between the jet axis angle, θ , and the electric vector position angle of all detected jet components. The distribution of quasars represents 73 measurements. The distribution of galaxies represents 7 sources. The distribution of BL Lacertae objects represents 17 measurements. The distribution of others includes 9 sources. The width of each bin is 3° .

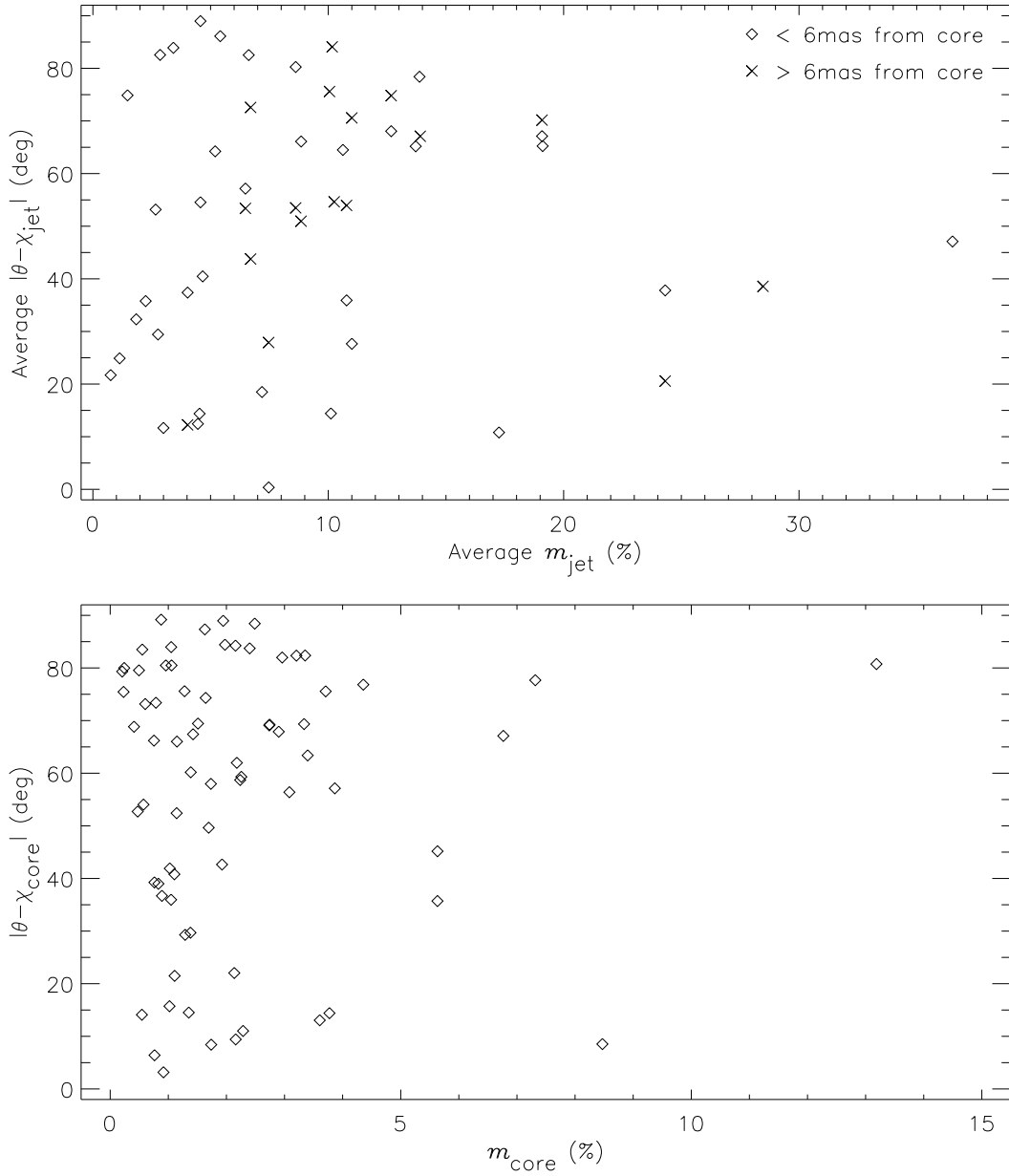


Fig. 11.— Top: Plot of the average difference between the jet axis angle, θ , and the electric vector position angle of all detected jet components nearer (\diamond) and farther (\times) than 6 mas from the core as a function of the average fractional polarization of the quasar jet. Only those quasars with detected jet polarizations are shown. 36 quasars are represented with the \diamond symbol and 17 are represented with the \times symbol. Bottom: Plot of the difference between the jet axis angle and the electric vector position angle in detected quasar cores as a function of core fractional polarizations.

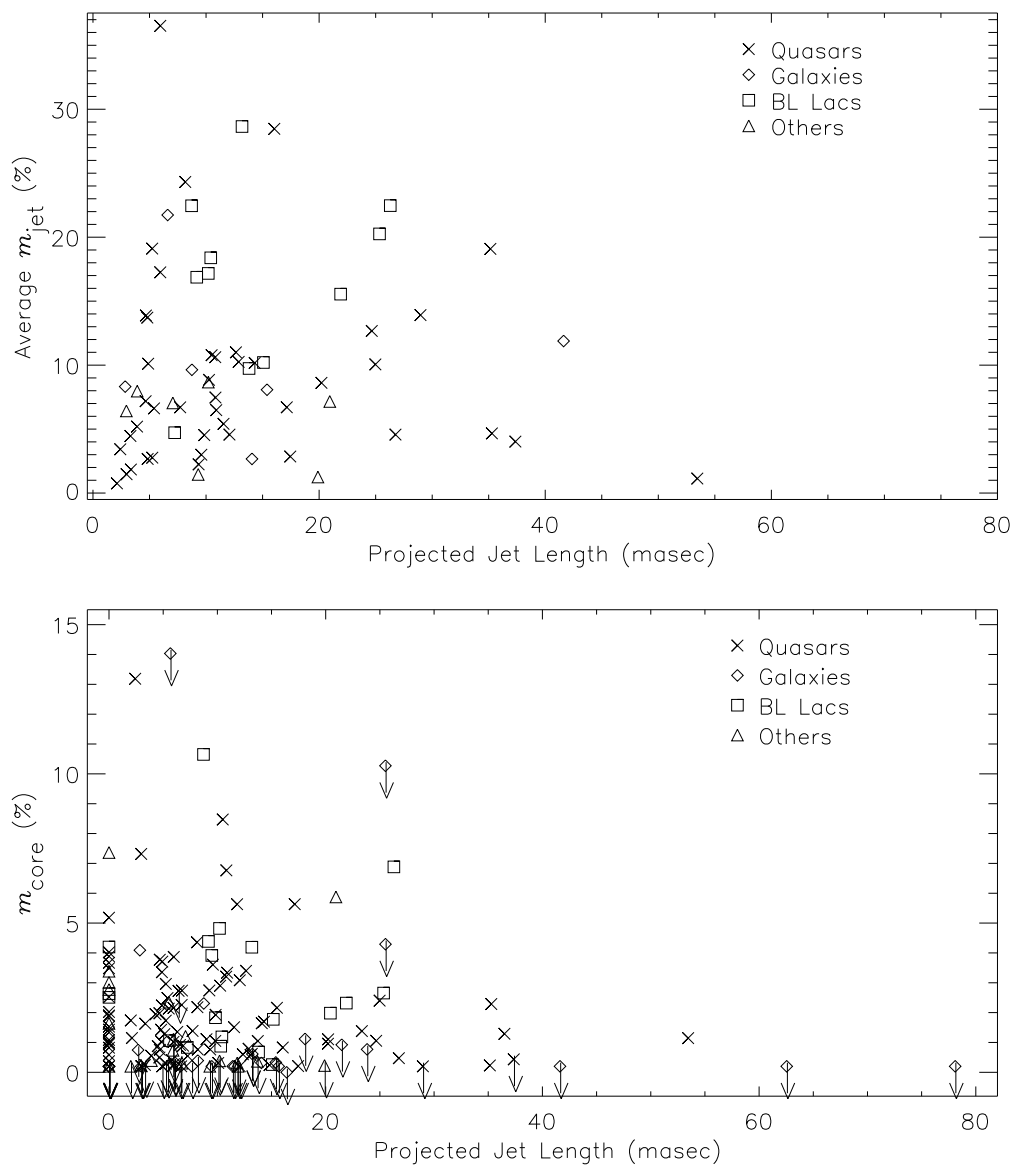


Fig. 12.— Plots of the average fractional polarizations of jet components (top) and the fractional core polarization (bottom) vs. projected jet length. The projected jet lengths and upper limits for the fractional core polarizations are calculated as described in § 3.3. The top plot shows 43 quasars, 6 galaxies, 11 BL Lacs and 7 others. The bottom plot shows data for 106 quasars, 30 galaxies, 20 BL Lacs and 21 others.

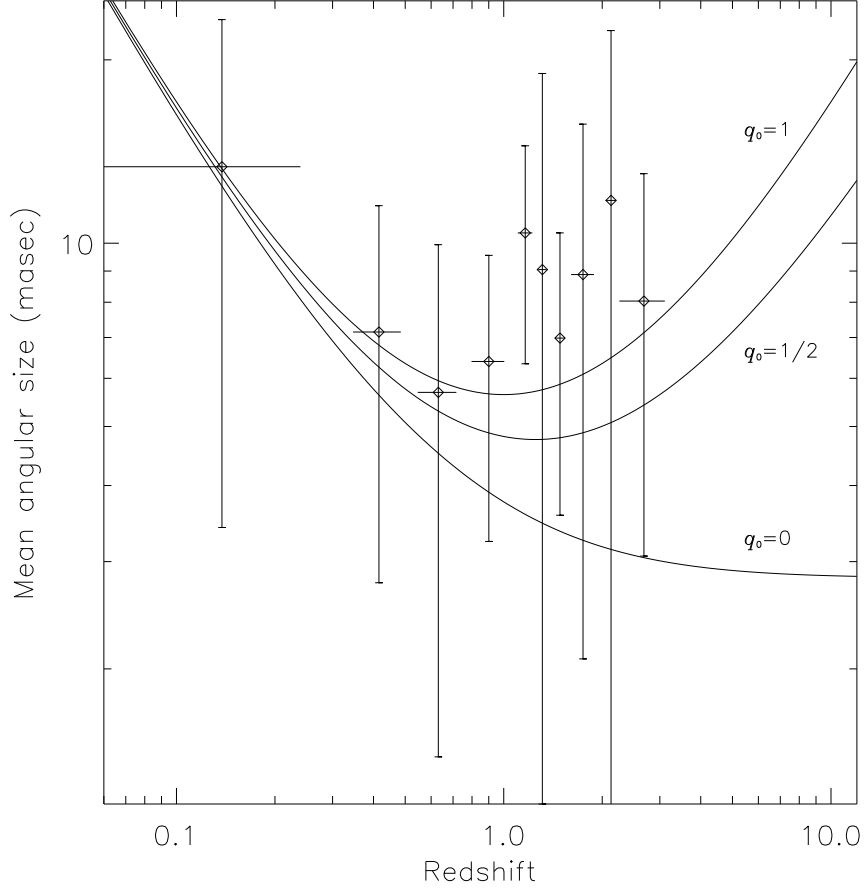


Fig. 13.— Plot of the redshift vs. uncorrected mean angular size in mas, where the mean angular size is calculated as described in § 3.3. Our definition of mean angular size mirrors the definition given in Kellermann (1993). Only those sources with core-jet morphologies and known redshifts are included. Additionally, BL Lacertae objects have been omitted to give a total of 103 sources. Each point represents roughly equal numbers of sources. (Starting with the lowest redshift bin, the bins contain 10, 10, 10, 11, 10, 10, 11, 10, 10 and 11 sources, respectively.) We show 1σ error bars, where σ_x is the standard deviation of the redshifts in each redshift bin, and σ_y is the standard deviation of the angular sizes in each redshift bin. The solid curves represent the theoretical dependence of angular size on redshift assuming a Friedmann cosmology with $H_0=50 \text{ km s}^{-1} \text{ Mpc}^{-1}$ and a source with an angular size of 41 parsecs.

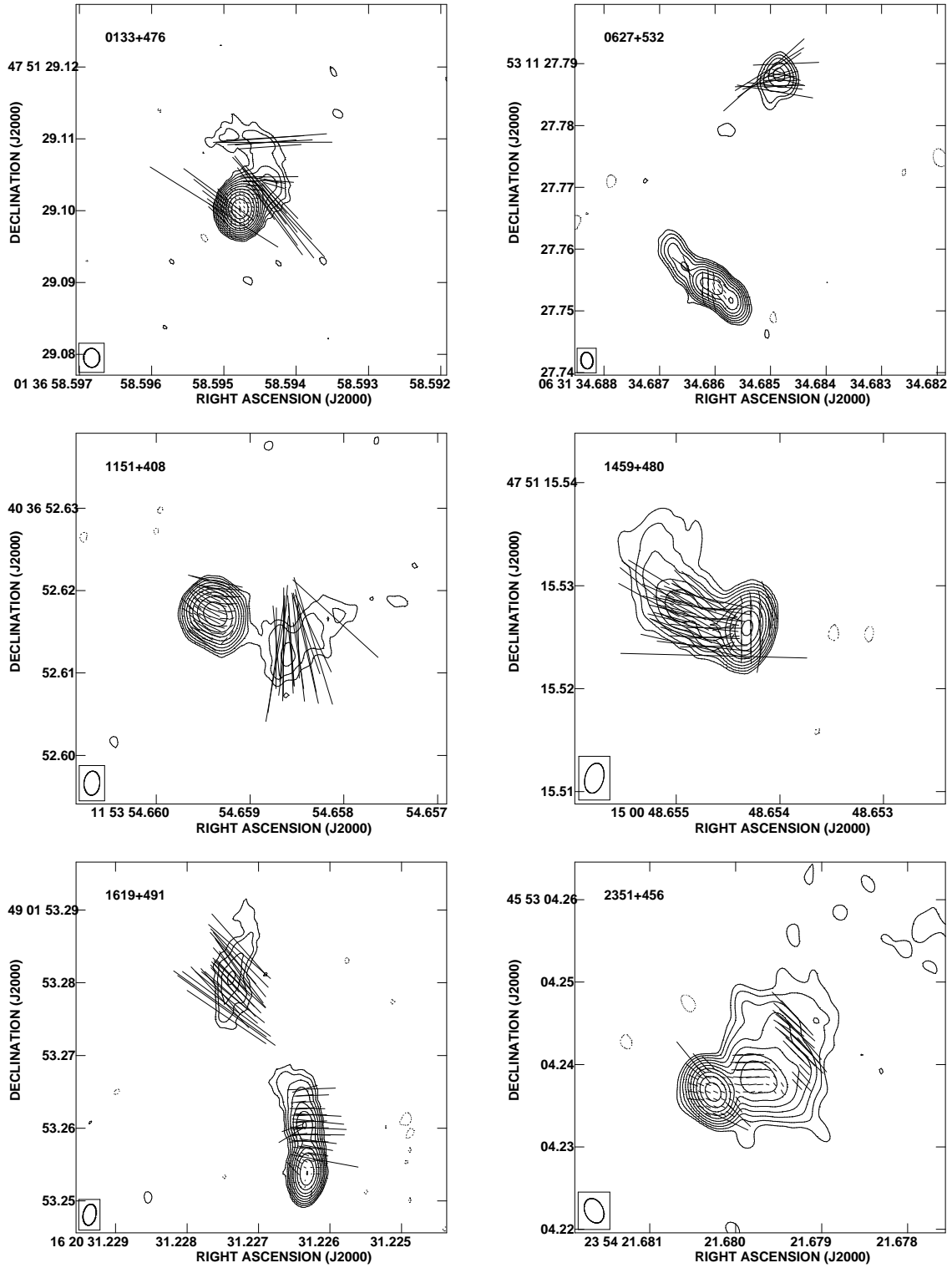


Fig. 14.— A selection of images from the sample showing those sources with moderate to large bends and some detected polarization. Contours, polarization vectors, and blanking is the same as Fig. 1.

TABLE 1
Measured Source Properties

| Source | E | P | C | θ_{axis} | I_{core}^* | p_{core}^* | χ_{core}^* | L | \bar{p}_{jet}^* | N* | F* | σ_I | σ_p |
|----------|-----|-----|-----------------|-----------------|--------------|--------------|-----------------|------|-------------------|------|------|------------|------------|
| (1) | (2) | (3) | (4) | (5) | (6) | (7) | (8) | (9) | (10) | (11) | (12) | (13) | (14) |
| 0003+380 | A | 2 | G _j | 122 | 545 | ≤1.1 | – | 11.6 | – | – | – | 0.18 | 0.10 |
| 0016+731 | C | P | Q _j | 3 | 298 | 3.8 | 79 | 5.1 | – | – | – | 0.22 | 0.11 |
| 0035+367 | C | E | Q _j | 41 | 92 | 0.9 | 25 | 6.0 | 17.3 | 11 | – | 0.15 | 0.11 |
| 0035+413 | A | 2 | Q _j | 108 | 322 | 2.5 | 2 | 12.9 | 10.3 | – | 55 | 0.12 | 0.10 |
| 0108+388 | C | P | G _c | 54 | 146 | ≤1.1 | – | 2.7 | – | – | – | 0.28 | 0.11 |
| 0109+351 | A | 2 | Q _n | – | 369 | 3.7 | 89 | – | – | – | – | 0.12 | 0.23 |
| 0110+495 | A | 2 | Q _j | 148 | 476 | 16.2 | 31 | 12.6 | 11.0 | 28 | 71 | 0.15 | 0.11 |
| 0133+476 | C | P | Q _j | 129 | 2248 | 23.6 | 33 | 9.8 | – | – | – | 0.26 | 0.14 |
| 0145+386 | A | 2 | Q _j | 100 | 286 | 6.5 | 41 | 6.7 | – | – | – | 0.19 | 0.09 |
| 0151+474 | A | 2 | O _n | – | 451 | 33.2 | 147 | – | – | – | – | 0.11 | 0.11 |
| 0153+744 | C | P | Q _j | 113 | 232 | ≤0.7 | – | 10.1 | – | – | – | 0.20 | 0.10 |
| 0212+735 | C | P | BL _j | 103 | 2405 | 16.3 | 164 | 13.8 | 9.7 | 59 | 64 | 0.54 | 0.20 |
| 0219+428 | A | E | BL _j | 170 | 612 | 14.2 | 164 | 21.9 | 15.5 | – | 33 | 0.15 | 0.13 |
| 0227+403 | A | 2 | Q _j | 130 | 285 | 10.8 | 144 | 4.7 | 13.9 | 78 | – | 0.11 | 0.10 |
| 0249+383 | A | 2 | Q _j | 158 | 345 | 7.5 | 96 | 8.2 | 24.3 | 38 | 21 | 0.12 | 0.09 |
| 0251+393 | A | 2 | Q _j | 82 | 217 | 1.8 | 121 | 16.0 | 28.5 | – | 39 | 0.10 | 0.10 |
| 0256+424 | B | 2 | O _j | 58 | 95 | ≤0.4 | – | 10.2 | 8.7 | 66 | 23 | 0.13 | 0.12 |
| 0307+380 | A | 2 | O _n | – | 707 | 19.6 | 121 | – | 8.7 | – | – | 0.10 | 0.12 |
| 0309+411 | A | 2 | G _j | 123 | 238 | ≤0.5 | – | 78.1 | – | – | – | 0.11 | 0.09 |
| 0316+413 | C | P | G _j | 178 | 2653 | ≤5.3 | – | 11.4 | – | – | – | 3.38 | 0.21 |
| 0340+362 | A | 2 | O _n | – | 340 | 5.6 | 45 | – | – | – | – | 0.10 | 0.10 |
| 0402+379 | B | 1 | G _c | 103 | 44 | ≤0.4 | – | 21.5 | – | – | – | 0.24 | 0.10 |
| 0454+844 | C | P | BL _n | – | 245 | 6.1 | 14 | – | – | – | – | 0.11 | 0.10 |
| 0537+531 | A | 2 | Q _j | 138 | 507 | 7.0 | 108 | 23.3 | – | – | – | 0.13 | 0.16 |
| 0546+726 | B | 2 | Q _j | 121 | 105 | ≤0.3 | – | 5.2 | 2.8 | 29 | – | 0.18 | 0.10 |
| 0554+580 | A | 2 | Q _j | 105 | 197 | 6.1 | 162 | 12.1 | 4.6 | 89 | – | 0.11 | 0.10 |
| 0600+442 | A | 2 | G _j | 122 | 141 | 0.4 | 86 | 14.1 | 2.7 | – | 62 | 0.16 | 0.11 |
| 0602+673 | B | 1 | Q _j | 16 | 1010 | 9.3 | 13 | 6.6 | – | – | – | 0.14 | 0.14 |
| 0604+728 | B | 2 | O _j | 115 | 131 | ≤0.3 | – | 19.9 | – | – | – | 0.27 | 0.10 |
| 0609+607 | A | 2 | Q _j | 143 | 572 | 11.3 | 48 | 4.7 | 7.2 | 18 | – | 0.13 | 0.12 |
| 0620+389 | B | 1 | Q _j | 135 | 350 | 19.7 | 0 | 17.1 | 6.7 | – | 73 | 0.12 | 0.11 |
| 0621+446 | A | E | BL _n | – | 174 | 4.6 | 136 | – | 6.7 | – | – | 0.09 | 0.10 |
| 0627+532 | A | 2 | Q _j | 52 | 81 | ≤0.4 | – | 37.4 | 4.2 | 37 | 39 | 0.15 | 0.12 |
| 0633+596 | A | 2 | O _j | 41 | 462 | ≤0.9 | – | 11.9 | – | – | – | 0.13 | 0.10 |
| 0641+393 | A | 2 | Q _j | 0 | 450 | 11.2 | 88 | 5.4 | 6.6 | 83 | – | 0.17 | 0.10 |
| 0642+449 | B | 1 | Q _j | 86 | 2076 | 18.2 | 175 | 4.5 | – | – | – | 0.18 | 0.28 |
| 0646+600 | A | 1 | Q _j | 37 | 640 | ≤1.3 | – | 3.0 | – | – | – | 0.19 | 0.11 |
| 0650+453 | A | 2 | Q _n | – | 193 | 1.8 | 137 | – | – | – | – | 0.10 | 0.10 |
| 0651+410 | A | 2 | G _n | – | 212 | ≤0.4 | – | – | – | – | – | 0.10 | 0.10 |

| Source | E | P | C | θ_{axis} | I_{core}^* | p_{core}^* | χ_{core}^* | L | \bar{p}_{jet}^* | N* | F* | σ_I | σ_p |
|----------|-----|-----|-----------------|-----------------|--------------|--------------|-----------------|------|-------------------|------|------|------------|------------|
| (1) | (2) | (3) | (4) | (5) | (6) | (7) | (8) | (9) | (10) | (11) | (12) | (13) | (14) |
| 0707+476 | B | 1 | Q _j | 27 | 531 | 29.9 | 62 | 11.8 | – | – | – | 0.10 | 0.10 |
| 0710+439 | C | P | G _c | 173 | 143 | ≤0.9 | – | 13.2 | – | – | – | 0.23 | 0.12 |
| 0711+356 | C | P | Q _j | 158 | 597 | 12.8 | 180 | 5.5 | – | – | – | 0.18 | 0.18 |
| 0714+457 | A | 2 | Q _j | 128 | 228 | 8.5 | 23 | 4.9 | – | – | – | 0.13 | 0.10 |
| 0716+714 | C | 1 | BL _j | 8 | 687 | 6.0 | 19 | 10.3 | – | – | – | 0.13 | 0.09 |
| 0724+571 | A | 2 | Q _j | 152 | 316 | 5.2 | 46 | 14.1 | – | – | – | 0.11 | 0.23 |
| 0727+409 | A | 2 | Q _j | 131 | 249 | 5.4 | 140 | 15.5 | – | – | – | 0.13 | 0.10 |
| 0731+479 | A | 2 | Q _j | 90 | 317 | ≤0.6 | – | 3.0 | – | – | – | 0.11 | 0.09 |
| 0738+491 | A | 2 | O _n | – | 458 | 13.8 | 68 | – | 0.9 | – | – | 0.14 | 0.11 |
| 0743+744 | A | 2 | Q _j | 24 | 223 | 3.9 | 82 | 5.2 | 19.1 | 65 | – | 0.11 | 0.10 |
| 0749+540 | A | 2 | BL _n | – | 1559 | 65.4 | 60 | – | 19.1 | – | – | 0.22 | 0.13 |
| 0800+618 | A | E | O _j | 131 | 738 | 17.3 | 50 | 5.5 | – | – | – | 0.16 | 0.12 |
| 0803+452 | A | 2 | Q _n | – | 257 | 2.5 | 32 | – | – | – | – | 0.11 | 0.09 |
| 0804+499 | C | P | Q _n | – | 570 | 8.7 | 99 | – | – | – | – | 0.15 | 0.12 |
| 0814+425 | C | P | BL _j | 126 | 858 | 9.1 | 85 | 5.6 | – | – | – | 0.31 | 0.14 |
| 0824+355 | A | 2 | Q _j | 49 | 420 | 2.4 | 175 | 13.1 | – | – | – | 0.15 | 0.13 |
| 0831+557 | C | P | G _j | 117 | 791 | ≤1.6 | – | 9.5 | – | – | – | 1.16 | 0.12 |
| 0833+416 | A | 2 | Q _j | 7 | 166 | 21.9 | 88 | 2.4 | 3.4 | 84 | – | 0.11 | 0.10 |
| 0836+710 | C | P | Q _j | 36 | 1292 | 3.0 | 111 | 35.2 | 19.1 | 67 | 70 | 0.41 | 0.16 |
| 0843+575 | A | 2 | O _j | 37 | 31 | ≤0.3 | – | 5.9 | – | – | – | 0.12 | 0.11 |
| 0847+379 | A | E | G _j | 3 | 169 | ≤0.3 | – | 6.6 | 21.7 | – | 37 | 0.09 | 0.09 |
| 0850+581 | C | P | Q _j | 152 | 600 | 6.3 | 8 | 13.7 | – | – | – | 0.14 | 0.12 |
| 0859+470 | C | P | Q _j | 0 | 371 | 4.2 | 128 | 53.5 | 1.1 | 25 | – | 0.20 | 0.14 |
| 0900+520 | A | 2 | Q _n | – | 165 | 5.8 | 168 | – | 1.8 | – | – | 0.10 | 0.09 |
| 0902+490 | A | 2 | Q _n | – | 483 | ≤1.0 | – | – | 1.8 | – | – | 0.15 | 0.09 |
| 0917+624 | C | 1 | Q _j | 162 | 1021 | 39.5 | 40 | 6.0 | – | – | – | 0.78 | 0.13 |
| 0923+392 | C | P | Q _n | – | 7902 | 105. | 59 | – | – | – | – | 1.49 | 0.34 |
| 0925+504 | A | 2 | BL _j | 135 | 415 | 44.2 | 51 | 8.7 | 22.5 | – | 15 | 0.14 | 0.10 |
| 0927+352 | A | 2 | Q _j | 103 | 242 | 8.7 | 90 | 9.6 | 3.0 | 12 | – | 0.12 | 0.10 |
| 0929+533 | A | 2 | Q _j | 131 | 241 | 5.2 | 47 | 6.0 | 36.5 | 47 | – | 0.11 | 0.09 |
| 0930+493 | A | 2 | Q _j | 45 | 260 | 19.0 | 147 | 3.0 | 1.5 | 75 | – | 0.12 | 0.10 |
| 0942+468 | A | 2 | G _n | – | 215 | ≤0.4 | – | – | 1.5 | – | – | 0.09 | 0.08 |
| 0945+408 | C | P | Q _j | 127 | 1180 | 28.3 | 31 | 25.0 | 10.1 | – | 76 | 0.26 | 0.27 |
| 0949+354 | A | 2 | Q _j | 167 | 343 | 4.8 | 47 | 7.7 | 6.7 | – | 44 | 0.25 | 0.09 |
| 0954+658 | C | P | BL _j | 106 | 311 | 12.2 | 122 | 9.5 | – | – | – | 0.13 | 0.11 |
| 1010+350 | A | 2 | G _j | 95 | 445 | 10.3 | 180 | 8.7 | 9.6 | 54 | 79 | 0.10 | 0.09 |
| 1030+398 | A | 2 | G _j | 45 | 372 | ≤0.7 | – | 3.0 | – | – | – | 0.10 | 0.10 |
| 1031+567 | C | P | G _c | 49 | 0 | ≤0.8 | – | 16.4 | – | – | – | 0.23 | 0.11 |
| 1038+528 | A | 2 | Q _j | 27 | 421 | 3.2 | 93 | 4.7 | – | – | – | 0.22 | 0.11 |
| 1041+536 | A | 2 | Q _j | 176 | 245 | 3.5 | 64 | 4.8 | 13.7 | 65 | – | 0.11 | 0.09 |
| 1058+726 | B | 1 | Q _j | 9 | 441 | 2.1 | 61 | 26.8 | 4.6 | 55 | – | 0.13 | 0.11 |

| Source | E | P | C | θ_{axis} | I_{core}^* | p_{core}^* | χ_{core}^* | L | \bar{p}_{jet}^* | N* | F* | σ_I | σ_p |
|----------|-----|-----|-----------------|-----------------|--------------|--------------|-----------------|------|-------------------|------|------|------------|------------|
| (1) | (2) | (3) | (4) | (5) | (6) | (7) | (8) | (9) | (10) | (11) | (12) | (13) | (14) |
| 1106+380 | A | E | O _j | 31 | 74 | ≤0.5 | – | 5.9 | – | – | – | 0.18 | 0.09 |
| 1124+455 | A | 2 | Q _j | 175 | 165 | ≤0.4 | – | 3.3 | 4.5 | 12 | – | 0.12 | 0.13 |
| 1144+352 | A | 2 | G _j | 122 | 58 | ≤0.4 | – | 23.8 | – | – | – | 0.13 | 0.14 |
| 1151+408 | A | 2 | Q _j | 59 | 229 | 19.4 | 68 | 10.5 | 10.8 | 36 | 54 | 0.12 | 0.09 |
| 1155+486 | A | 2 | Q _j | 69 | 327 | 9.0 | 0 | 6.7 | – | – | – | 0.15 | 0.11 |
| 1205+544 | A | 2 | O _j | 117 | 116 | 0.4 | 105 | 6.7 | – | – | – | 0.12 | 0.10 |
| 1206+415 | A | 2 | BL _j | 12 | 162 | 3.0 | 26 | 9.8 | – | – | – | 0.09 | 0.09 |
| 1221+809 | A | 2 | BL _j | 173 | 353 | 15.5 | 121 | 9.2 | 16.9 | 37 | 43 | 0.13 | 0.10 |
| 1223+395 | A | 2 | G _j | 34 | 118 | ≤0.4 | – | 15.4 | 8.1 | – | 85 | 0.12 | 0.09 |
| 1226+373 | A | 2 | Q _j | 105 | 362 | 1.8 | 25 | 4.7 | – | – | – | 0.09 | 0.09 |
| 1239+376 | A | 2 | Q _n | – | 253 | 10.2 | 139 | – | – | – | – | 0.11 | 0.09 |
| 1240+381 | A | 2 | Q _j | 87 | 510 | 3.1 | 160 | 12.4 | – | – | – | 0.20 | 0.09 |
| 1250+532 | A | 2 | BL _j | 79 | 174 | 2.1 | 78 | 10.4 | 18.4 | 5 | 1 | 0.13 | 0.09 |
| 1258+507 | A | 2 | Q _j | 170 | 184 | 2.4 | 19 | 36.5 | – | – | – | 0.11 | 0.09 |
| 1305+804 | A | E | O _j | 61 | 76 | ≤0.3 | – | 13.7 | – | – | – | 0.10 | 0.09 |
| 1306+360 | A | E | Q _n | – | 376 | 7.1 | 20 | – | – | – | – | 0.10 | 0.14 |
| 1308+471 | A | 2 | Q _n | – | 220 | 8.6 | 103 | – | – | – | – | 0.10 | 0.11 |
| 1312+533 | A | 2 | O _j | 63 | 275 | ≤0.6 | – | 2.0 | – | – | – | 0.15 | 0.10 |
| 1321+410 | A | 2 | G _j | 96 | 158 | ≤0.4 | – | 5.4 | – | – | – | 0.19 | 0.10 |
| 1325+436 | A | 2 | Q _j | 56 | 230 | 2.1 | 20 | 6.8 | – | – | – | 0.09 | 0.09 |
| 1355+441 | A | E | G _c | 122 | 2 | ≤0.3 | – | 5.7 | – | – | – | 0.17 | 0.09 |
| 1356+478 | A | E | G _j | 70 | 121 | ≤0.4 | – | 6.1 | – | – | – | 0.12 | 0.09 |
| 1413+373 | A | 2 | Q _j | 115 | 180 | 3.5 | 24 | 4.3 | – | – | – | 0.13 | 0.09 |
| 1415+463 | A | 2 | Q _j | 81 | 237 | 7.9 | 150 | 10.9 | 6.5 | 57 | 53 | 0.11 | 0.09 |
| 1417+385 | A | 2 | Q _n | – | 1301 | 47.7 | 124 | – | 6.5 | – | – | 0.12 | 0.13 |
| 1421+482 | A | 2 | Q _j | 100 | 108 | 1.8 | 13 | 3.4 | 1.8 | 32 | – | 0.09 | 0.09 |
| 1424+366 | A | 2 | Q _n | – | 406 | 5.8 | 78 | – | 1.8 | – | – | 0.12 | 0.14 |
| 1427+543 | A | 2 | Q _j | 135 | 390 | 12.5 | 53 | 10.8 | 10.6 | 64 | – | 0.18 | 0.26 |
| 1432+422 | A | E | O _n | – | 196 | 6.7 | 179 | – | 10.6 | – | – | 0.11 | 0.09 |
| 1448+762 | A | 2 | G _n | – | 248 | ≤0.5 | – | – | 10.6 | – | – | 0.11 | 0.09 |
| 1456+375 | A | 2 | G _j | 108 | 113 | 4.6 | 158 | 2.8 | 8.3 | 1 | – | 0.09 | 0.09 |
| 1459+480 | A | 2 | BL _j | 86 | 274 | 13.2 | 4 | 10.2 | 17.2 | 0 | 13 | 0.10 | 0.10 |
| 1505+428 | A | 2 | G _j | 81 | 420 | ≤0.8 | – | 7.6 | – | – | – | 0.11 | 0.10 |
| 1534+501 | A | 2 | Q _n | – | 133 | 2.5 | 165 | – | – | – | – | 0.11 | 0.12 |
| 1543+480 | A | 2 | G _j | 114 | 257 | ≤0.5 | – | 62.5 | – | – | – | 0.12 | 0.09 |
| 1543+517 | A | 2 | Q _j | 0 | 326 | 3.4 | 80 | 24.7 | 12.7 | 68 | 75 | 0.11 | 0.09 |
| 1550+582 | A | 2 | Q _n | – | 201 | ≤0.4 | – | – | 12.7 | – | – | 0.13 | 0.09 |
| 1619+491 | A | 2 | Q _j | 3 | 229 | ≤0.5 | – | 29.0 | 13.9 | – | 67 | 0.12 | 0.10 |
| 1622+665 | A | E | G _n | – | 232 | ≤0.5 | – | – | 13.9 | – | – | 0.10 | 0.09 |
| 1623+578 | A | E | O _j | 67 | 316 | 18.6 | 110 | 20.9 | 7.2 | 54 | – | 0.12 | 0.10 |
| 1624+416 | C | P | Q _j | 172 | 329 | ≤0.7 | – | 6.7 | – | – | – | 0.20 | 0.12 |

| Source | E | P | C | θ_{axis} | I_{core}^* | p_{core}^* | χ_{core}^* | L | \bar{p}_{jet}^* | N* | F* | σ_I | σ_p |
|----------|-----|-----|-----------------|-----------------|--------------|--------------|-----------------|------|-------------------|------|------|------------|------------|
| (1) | (2) | (3) | (4) | (5) | (6) | (7) | (8) | (9) | (10) | (11) | (12) | (13) | (14) |
| 1636+473 | A | 2 | Q _j | 156 | 617 | 4.7 | 15 | 8.2 | – | – | – | 0.20 | 0.10 |
| 1637+574 | C | P | Q _j | 23 | 734 | 4.1 | 119 | 3.9 | 5.2 | 64 | – | 0.19 | 0.13 |
| 1638+540 | A | 2 | Q _n | – | 205 | 5.2 | 158 | – | 6.6 | – | – | 0.10 | 0.09 |
| 1641+399 | C | P | Q _j | 114 | 6798 | 75.1 | 73 | 20.2 | – | – | – | 0.97 | 0.77 |
| 1642+690 | C | P | Q _j | 21 | 447 | 13.0 | 133 | 10.3 | 8.8 | 66 | 51 | 0.17 | 0.14 |
| 1645+410 | A | 2 | Q _n | – | 341 | 1.3 | 58 | – | 9.4 | – | – | 0.11 | 0.10 |
| 1652+398 | A | P | BL _j | 126 | 537 | 1.4 | 166 | 15.1 | 10.2 | 60 | 48 | 0.24 | 0.10 |
| 1722+401 | A | 2 | Q _j | 118 | 327 | ≤0.7 | – | 12.1 | – | – | – | 0.11 | 0.09 |
| 1726+455 | A | 2 | Q _j | 90 | 1075 | 29.5 | 159 | 9.3 | – | – | – | 0.13 | 0.12 |
| 1738+499 | A | 2 | Q _j | 0 | 300 | 4.1 | 165 | 6.3 | – | – | – | 0.10 | 0.09 |
| 1739+522 | C | P | Q _j | 52 | 551 | ≤1.1 | – | 4.9 | – | – | – | 0.15 | 0.12 |
| 1744+557 | A | E | G _j | 68 | 182 | ≤0.4 | – | 15.7 | – | – | – | 0.10 | 0.10 |
| 1746+470 | A | 2 | Q _n | – | 457 | 2.7 | 180 | – | – | – | – | 0.14 | 0.22 |
| 1747+433 | A | 2 | BL _j | 168 | 135 | 5.6 | 35 | 13.2 | 28.6 | – | 13 | 0.11 | 0.11 |
| 1749+701 | C | P | BL _j | 133 | 359 | 3.0 | 79 | 7.2 | 4.7 | 34 | – | 0.15 | 0.12 |
| 1755+578 | A | 2 | Q _j | 75 | 58 | ≤0.4 | – | 13.2 | – | – | – | 0.11 | 0.10 |
| 1803+784 | C | P | BL _j | 83 | 1780 | 122. | 97 | 26.3 | 22.5 | 5 | 41 | 0.74 | 0.16 |
| 1807+698 | C | P | G _j | 78 | 747 | ≤1.5 | – | 41.6 | 11.9 | – | 15 | 0.18 | 0.13 |
| 1812+412 | A | 2 | Q _j | 82 | 222 | 3.8 | 132 | 14.3 | 10.2 | – | 84 | 0.11 | 0.10 |
| 1823+568 | C | P | BL _j | 18 | 629 | 16.7 | 12 | 25.3 | 20.3 | – | 12 | 0.16 | 0.15 |
| 1828+399 | A | 2 | O _n | – | 157 | ≤0.3 | – | – | 13.0 | – | – | 0.09 | 0.09 |
| 1839+389 | A | 2 | Q _n | – | 196 | 1.6 | 95 | – | 13.0 | – | – | 0.09 | 0.09 |
| 1842+681 | A | 1 | Q _j | 131 | 342 | 5.2 | 21 | 11.5 | 5.4 | 86 | – | 0.14 | 0.14 |
| 1850+402 | A | 2 | Q _j | 63 | 407 | 7.1 | 72 | 2.0 | – | – | – | 0.13 | 0.10 |
| 1851+488 | A | 2 | Q _n | – | 248 | 5.0 | 144 | – | – | – | – | 0.12 | 0.13 |
| 1908+484 | A | 2 | O _j | 60 | 96 | ≤0.3 | – | 11.8 | – | – | – | 0.10 | 0.10 |
| 1910+375 | A | 2 | Q _j | 176 | 268 | 11.7 | 73 | 8.1 | 20.1 | – | 76 | 0.13 | 0.83 |
| 1924+507 | A | 2 | Q _j | 0 | 217 | 1.7 | 6 | 9.3 | 2.2 | 36 | – | 0.11 | 0.11 |
| 1928+738 | C | P | Q _j | 159 | 1664 | 15.9 | 79 | 20.2 | 8.6 | 80 | 53 | 0.66 | 0.18 |
| 1943+546 | A | 1 | G _c | 84 | 14 | ≤0.6 | – | 25.5 | – | – | – | 0.24 | 0.09 |
| 1946+708 | A | 2 | G _c | 32 | 29 | ≤0.3 | – | 18.1 | – | – | – | 0.31 | 0.09 |
| 1954+513 | C | P | Q _j | 125 | 580 | 1.4 | 45 | 14.8 | – | – | – | 0.18 | 0.12 |
| 2021+614 | C | P | Q _c | 41 | 91 | ≤2.5 | – | 6.4 | – | – | – | 0.36 | 0.18 |
| 2054+611 | A | 2 | O _j | 165 | 253 | 3.0 | 12 | 7.1 | 7.0 | 62 | 83 | 0.12 | 0.11 |
| 2116+818 | A | E | G _j | 153 | 72 | ≤0.3 | – | 8.2 | – | – | – | 0.12 | 0.09 |
| 2136+824 | A | 2 | Q _j | 139 | 117 | 2.7 | 128 | 35.3 | 5.1 | 40 | 40 | 0.18 | 0.12 |
| 2138+389 | B | 2 | Q _j | 90 | 124 | ≤0.3 | – | 6.0 | – | – | – | 0.13 | 0.11 |
| 2200+420 | C | P | BL _j | 162 | 1098 | 19.5 | 170 | 15.2 | – | – | – | 0.35 | 0.16 |
| 2214+350 | A | 1 | Q _j | 7 | 346 | 1.9 | 173 | 7.3 | – | – | – | 0.12 | 0.10 |
| 2235+731 | A | 2 | O _j | 32 | 287 | 1.1 | 106 | 3.9 | 8.0 | 57 | – | 0.11 | 0.10 |
| 2238+410 | A | 2 | Q _j | 133 | 320 | 7.2 | 11 | 4.9 | – | – | – | 0.11 | 0.10 |

| Source | E | P | C | θ_{axis} | I_{core}^* | p_{core}^* | χ_{core}^* | L | \bar{p}_{jet}^* | N* | F* | σ_I | σ_p |
|----------|-----|-----|----------------|-----------------|--------------|--------------|-----------------|------|-------------------|------|------|------------|------------|
| (1) | (2) | (3) | (4) | (5) | (6) | (7) | (8) | (9) | (10) | (11) | (12) | (13) | (14) |
| 2310+385 | A | 2 | Q _j | 60 | 202 | 2.1 | 102 | 4.8 | 2.7 | 53 | – | 0.10 | 0.11 |
| 2319+444 | A | 2 | Q _n | – | 303 | 15.7 | 134 | – | 2.7 | – | – | 0.11 | 0.10 |
| 2346+385 | A | 2 | Q _j | 149 | 344 | 10.2 | 51 | 5.2 | – | – | – | 0.14 | 0.10 |
| 2351+456 | C | P | Q _j | 108 | 768 | 14.8 | 66 | 9.8 | 4.5 | 14 | – | 0.25 | 0.18 |
| 2352+495 | A | P | G _c | 2 | 8 | ≤0.9 | – | 25.5 | – | – | – | 0.33 | 0.09 |
| 2356+385 | A | 2 | Q _n | – | 329 | 3.6 | 24 | – | – | – | – | 0.12 | 0.10 |
| 2356+390 | A | 2 | Q _j | 51 | 125 | 8.5 | 164 | 10.8 | 7.5 | 0 | 28 | 0.09 | 0.09 |

*A more complete table with all measured source properties, including jet components, can be found at www.aoc.nrao.edu/~gtaylor/cjftab.text.

Note. — Col. (1): B1950 source name. Col. (2): E, epoch – A:1998; B:1999; C:2000. Col. (3): P, parent sample – P:Pearson & Readhead 1988; 1: first Caltech-Jodrell Bank survey (CJ1, Polatidis et al. 1995); 2: second Caltech-Jodrell Bank survey (CJ2, Taylor et al. 1994); E: 18 sources not included in PR, CJ1 or CJ2 that complete the Caltech-Jodrell Bank flat-spectrum survey (CJF). Col. (4): C, class. Key to identifications: Q:quasar; G:galaxy; BL:BL Lac object; O:other. Key to subscripts: j:core-jet morphology; n:naked core morphology; c:Compact Symmetric Object. Col. (5): jet axis angle (deg). Col. (6): total intensity at the core (mJy). Col. (7): total polarized intensity at the core (mJy); cores with detected polarized intensities have $1\sigma_{\text{typical}} \approx 0.2$ mJy. Col. (8): electric vector position angle at the core (deg); cores that meet detection criteria have $1\sigma_{\text{typical}} \approx 4^\circ$. Col. (9): L, jet length (mas). Col. (10): average polarized intensity of detected jet components (mJy). Col. (11): N, average difference between jet axis angle and electric vector position angle in detected jet components within 6 mas of the core (deg). Col. (12): F, average difference between jet axis angle and electric vector position angle in detected jet components farther than 6 mas from the core (deg). Col. (13): total intensity RMS noise (mJy). Col. (14): polarized intensity RMS noise (mJy).